Diagenetic overprint on negative $\delta^{13}C$ excursions across the Permian/Triassic boundary: A case study from Meishan section, China

Rong Li*

State Key Laboratory of Biogeology and Environmental Geology, China University of Geosciences, Wuhan, 430074, China

*Corresponding author, E-mail: rongli_cug@163.com

Abstract

The Meishan Section D from China is the Global Stratotype Section and Point (GSSP) of the Permian-Triassic boundary (PTB). In this section and laterally correlatable Section A, diagenetic features of Beds 24 to 62 are examined in this study to determine the negative shift in $\delta^{13}C_{carb}$ across the Permian-Triassic boundary is diagenetic in origin or not. Bed 24 is formed of skeletal packstones, while Beds 25 to 62 are formed of either claystones, or mudstones and/or calcareous mudstones with dolomite being present. The dolomite crystals are typically < 30 μm long, subhedral to euhedral, held in very fine groundmass. The cathodoluminescent features and backscattered images show that the dolomite crystals have zoned internal architecture, with a non-luminescent low-calcium calcian dolomite (LCD) core being encased successively by an irregular dull-orange calcite zone, an euhedral bright-orange high-calcium calcian dolomite (HCD) cortex, and the outmost ferroan-HCD zone.

The limestones in Bed 24 display $\delta^{13}C$ values ranging from 1.72 to 2.92‰, $\delta^{18}O$ values from –7.74 to –4.84‰. In Beds 25 to 62, the dolomites have $\delta^{13}C$ values between -1.47 and 4.11‰, $\delta^{18}O$ values between –7.38 and –1.79‰, whereas the coexisting calcites have $\delta^{13}C$ values from –1.52 to 2.05‰, $\delta^{18}O$ values from –10.24 to –3.33‰. The bulk samples of Bed 24 yielded Sr concentrations of 404 to 857 ppm (average 590 ppm), the Sr content of brachiopod shells varies between 746 and 837 ppm (average 780 ppm), whereas the Sr in dolomite is generally less than 300 ppm. The PAAS-normalized REY patterns of samples from Bed 24 are seawater-like, whereas those of brachiopod shells are LREE enriched relative to HREE, those of dolomite are MREE enriched. Available evidence indicates that the zoned dolomite crystals formed episodically. After their syndepositional precipitation, the euhedral HCD underwent modifications including calcitization by meteoric water, re-

dolomitization of calcite, and overgrowth of ferroan dolomite. The dramatically negative $\delta^{13}C$ excursions of calcite in Beds 26 and 28 are related to meteoric diagenesis, while the negative $\delta^{13}C$ excursions of calcite in dolomite-bearing beds are ascribed to enriched ^{12}C resulted from dolomitization mediated by sulfate reducing bacterial (SRB) in burial process.

The results show that the $\delta^{13}C$ signals recorded in the global stratotype section that spans the PTB is not primary in origin. The synchronistic negative shift in $\delta^{13}C$ signals across the PTB are partly contributed by diagenesis. Hence, diagenetic alteration needs to be considered before using $\delta^{13}C_{carb}$ to estimate the dissolved inorganic carbon in the ancient oceans and to calculate the global carbon cycle.

Key words: Permian/Triassic boundary, diagenesis, Meishan, $\delta^{13}C$ excursion, dolomitization

1. INTRODUCTION

Given that the mass extinction event at the Permian-Triassic boundary (hereafter referred to as PTB) was the biggest in the Phanerozoic Era, the associated carbonate successions have long been studied in an effort to determine the extinction mechanisms. Such studies have shown that the stable inorganic carbon isotope displays a world wide significant negative shift across the PTB sections (Baud et al., 1989; Holser et al., 1989), which were deposited in settings ranging from continental platform (e.g., Pufels section and Tesero section from Italy, Broglio Loriga and Cassinis, 1992; Horacek et al., 2007; Kearsey et al., 2009; Korte and Kozur, 2010) to ramps (e.g., Meishan section from South China, Abadeh section from central Iran, Jin et al., 2000; Heydari et al., 2003; Korte et al., 2004; Korte and Kozur, 2010; Yin et al., 2014) to deep basins (Shangsi section from South China, Jiang et al., 2011; Song et al., 2012) (Fig. 1). The extinction event horizon is lower than the PTB (Fig. 1), which is defined as the first appearance of the conodont species *Hindeodus parvus* (Yin et al., 2001). The Triassic baseline is depleted ~ 4 − 7‰ in $\delta^{13}C$ relative to the Permian baseline (Fig. 1). In general, the negative shift commenced in the late Changhsingian *Clarkina yini* Zone, first peaked near the extinction event horizon (*C. meishanensis* Zone), then peaked in the early Griesbachian *H. parvus* Zone and *Isarcicella isarcica* Zone after a few positive shift (Fig. 1, Kearsey et al., 2009; Korte and Kozur, 2010; Song et al., 2013; Yin et al., 2014). The synchronistic negative shift in $\delta^{13}C$ in the PTB intervals has generally been attributed to a synchronistic shift in the $\delta^{13}C$ of the global carbon cycle (e.g., Korte et al., 2004; Korte and Kozur, 2010). This assertion is based on the assumption that the $\delta^{13}C$ signals recorded in the carbonate succession are primary in origin. Several lines of evidence listed below, however, suggest that the $\delta^{13}C$ signals may, at least in part, reflect secondary diagenetic processes. Specifically, the following issues need to be considered.

- There was a significant global regression at the end of Permian (Newell, 1967; Holser and Magaritz, 1987). In theory, long-term exposure of carbonate rocks in the meteoric vadose environment during the sea-level lowstands can produce distinctive negative shift in $\delta^{13}C$ (Allan and Matthews, 1982).
- Heydari et al. (2001) argued that the abrupt lithology change across the PTB was caused by subaerial exposure and associated stratigraphy hiatus. Recent work by Yin et al. (2014) supported the conclusion reached by Heydari et al. (2001). After examination of conodont distribution patterns in the Permian-Triassic carbonate succession of the basinal facies and platform facies in South China, Yin et al. (2014) pointed out that the conodont zones are continuous in the basinal succession but discontinuous in the platform succession. In the platform succession, the missing conodont zones at the PTB result from the depositional hiatus that was associated with the Late Permian drop in sea level at the *Clarkina meishanensis* zone to *Hindeodus changxingensis* zone (Yin et al., 2014). The unconformity at the PTB has long been attributed to subaerial exposure and associated karstification that took place during a sea-level drop (Wu et al., 2006; Collin et al., 2009; Wignall et al., 2009). The above evidence of sea-level lowstand provides the theoretical possibility that both the $\delta^{13}C$ and $\delta^{18}O$ signal in the uppermost Permian beds may have been modified by meteoric diagenesis.
- Recent studies by Swart (2008), Swart and Kennedy (2012), and Oehlert and Swart (2014) on Pliocene-Pleistocene island carbonate successions have verified

that a globally synchronistic change in $\delta^{13}C$ could be ascribed to meteoric diagenesis that takes place in response to a fall in sea-level.

- Burial diagenesis could generate the anomalously low $\delta^{13}C$ as well. For example, the marked negative $\delta^{13}C$ excursions in Ediacaran-age carbonates, which have been identified in several sections globally, have been attributed to fluid-rock and fluid-fluid interactions during burial diagenesis (Derry, 2010).

Collectively, this information raises the possibility that the abrupt negative shift in the $\delta^{13}C$ evident in global Permian/Triassic boundary sections may be caused by the meteoric diagenesis that was associated with the sea-level drop and/or the post-depositional burial diagenesis rather than a global shift in the carbon cycle.

In order to test the hypothesis that diagenesis (meteoric and/or burial) may, at least in part, be responsible for the change in the $\delta^{13}C$ signal, the detailed diagenetic features of PTB interval in the Meishan Section are first presented in this study. Then, the trends in $\delta^{13}C$ and $\delta^{18}O$ profiles in the Meishan section are compared with other PTB sections to show that the negative shift in $\delta^{13}C$ was diagenetic in origin. The Meishan section was selected for study because (1) it is the Global Stratotype Section and Point (GSSP) for the Permian–Triassic boundary and records the continuous deposition in the Permian/Triassic transitional period, (2) the ages of critical intervals across the Permian–Triassic boundary are known (Shen et al., 2011; Burgess et al., 2014) and conodont biostratigraphy is well established (Jiang et al., 2007), (3) the results will fill in gaps in the known diagenetic features of the GSSP Meishan section and thereby allow comparison with diagenetic work on global Permian–Triassic boundary sections (Heydari et al., 2000, 2001; Collin et al., 2009; Wu et al., 2014), and (4) adequate samples are available for the study. The results indicate that diagenetic alteration needs to be considered before using $\delta^{13}C_{carb}$ to estimate the dissolved inorganic carbon in the ancient oceans and to calculate the global carbon cycle. These results may also help to explain the $\delta^{13}C$ excursions found in other geological boundaries, such as Jurassic–Cretaceous boundary (Hermoso et al., 2009) and the Cretaceous–Tertiary boundary.

2. TERMINOLOGY

Argillaceous carbonate rocks are carbonate sediments that include 10 – 40% clay minerals. For the argillaceous carbonates of mixed calcite and dolomite, they are named argillaceous dolostone if the dolomite content exceeds the calcite content, otherwise they are named as argillaceous dolomitic limestone. Micrite is used for crystals that are < 4 μm long, and microspar for crystals that are 4 – 30 μm long (cf. Folk, 1959).

Following Jones and Luth (2002), the dolomite is divided into low-Ca calcian dolomite (LCD) and high-Ca calcian dolomite (HCD) according to the mol % $CaCO_3$ content of dolomite (molar Ca/(Ca + Mg) ×100, hereafter referred to as %Ca following Jones and Luth, 2002). By definition, LCD contains < 55 %Ca, whereas HCD contains > 55 %Ca (Jones and Luth, 2002). Ferroan calcite refers to calcite with a Fe concentration over 200 ppm (Muchez et al., 1994), whereas the ferroan dolomite contains 5% to 10% mol % $FeCO_3$ (Reinhold, 1998, his Figure 5).

3. GEOLOGICAL SETTING

The Meishan quarry, located about 20 km northwest of Changxing County in Zhejiang Province, has good exposures of the PTB in sections A, B, C, D, E, and Z, which are distributed over a distance of about 2 km (Fig. 2). There, Section D, which includes, in ascending order, the Longtan Formation, the Changhsing Formation, the

Yinkeng Formation, the Helongshan Formation, and the Nanlinghu Formation (Fig. 3), is the Global Stratotype Section and Point (GSSP) of the Permian and Triassic boundary. The Permian-Triassic stratigraphic succession is divided into 115 beds (Zhang et al., 2005), with the Changhsingian Changhsing Formation (40.42 m thick) consisting of Beds 2 to 24 and the early Griesbachian Yinkeng Formation (14.1 m thick) consisting of Beds 25 to 60 (Fig. 3). In general, the Changhsing Formation is formed mainly of skeletal packstones, with various skeletal grains such as foraminifers, ostracods, and sponge spicules being present along with numerous brachiopod fragments (Chen et al., 2015). In contrast, the Yinkeng Formation has fewer skeletal grains and consists mainly of mudstone in the basal part (Beds 25 to 30), laminated calcareous mudstone in the lower part (Beds 31 to 53), and alternating beds of mudstone and calcareous mudstone is the upper part (Beds 54 to 60) (Zhang et al., 2005; Fig. 4).

The PTB is placed 8 cm above the base of Bed 27, which is about 16 cm thick, and sandwiched between clay beds (Fig. 4). Hence, Bed 27 is the boundary carbonate, whereas the clay beds below and above are the boundary clay beds. Zhang et al. (1997) divided Bed 27 in Section D into 27a, 27b, 27c, and 27d in ascending order, with the PTB being at the bottom of 27c. The succession in Section D can be matched with the other sections in the quarry (Tong et al., 1996). Available evidence suggests that the Permian/Triassic carbonate succession in the Meishan section was probably deposited in a carbonate ramp with water depth ~ 100 − 200 m (Feng et al., 1997; Zhang et al., 1997, 2005; Cao and Zheng, 2009; Zheng et al., 2013; Chen et al., 2015).

4. METHODS

This study focused on the diagenetic features in the stratigraphic interval between Bed 24 and Bed 62, which covers the negative shift in $\delta^{13}C$ from the late Changhsingian *C. yini* Zone to the early Griesbachian *I. isarcica* Zone. .

Samples came from one core drilled in Meishan Section D and hand samples collected from Section A, which are about 1.2 km apart (Fig. 1A). Seven polished rock samples, two large polished thin sections, and 36 regular polished thin sections were made from these samples. Seventy powdered bulk samples (each weighing about 5 g) covering beds 24 to 62 were analyzed on a Panalytical X'Pert Pro Powder XRD system that was run at 40 kV and 40 mA using a X'Pert Pro X-ray generator with a Cu tube and Ni filter. All scans were run from 3º to 65º 2θ at a speed of 0.417782º/s. The mineralogy composition was calculated semi-quantitatively using the K-value method (Chung, 1974). The values obtained using this method are accurate at ± 5 wt.%.

The matrices surrounding the allochems are so fine (< 30 μm) that the petrographic observation of diagenetic features were determined under scanning electron microscope (SEM) and cathodoluminescence (CL) microscope. Backscattered electron (BSE) images were generated from polished samples coated with carbon on a FEI Quanta 450 FEG field emission SEM equipped with electron backscattered diffraction (EBSD) at 20 kV, 20 nA, as 1024 × 943 pixel maps. The elemental contents of the crystals were obtained by using the energy dispersive X-ray (EDX) analyzer that is attached to the SEM. Polished thin sections were examined with CL microscopy. A Technosyn Model 8200 Mark V cold-cathode instrument was mounted on a Leica DM2500 P Polarization Microscope equipped with a Leica

DFC300FX digital camera. Operating voltages were 12.1 kV and gun current levels were 198 μA.

The stable oxygen and carbon isotope of samples with mixed dolomite and calcite (n = 39) were determined at the Stable Isotope Laboratory in the University of Alberta, following the protocol described by McCrea (1950). The evolved gases were analyzed on a Finnigan MAT 251 mass spectrometer. Isotopic values are reported as per mil relative to the Vienna Pee Dee Belemnite (VPDB) standard. The precision (standard error, 1 sigma) for both $\delta^{13}C$ and $\delta^{18}O$ was ± 0.1‰. The oxygen isotope values of the dolomite were not corrected for the phosphoric acid fractionation. The stable oxygen and carbon isotopic compositions for bulk samples (n = 48) were carried out in the State Key Laboratory of Biogeology and Environmental Geology, China University of Geosciences at Wuhan. For each sample, the powder (weighing 150 – 400 μg) was reacted with 100% phosphoric acid at 72ºC after flushing with helium, and the evolved CO_2 was analyzed on a Finnigan MAT 253. Analytical precision was better than ± 0.1‰ for both $\delta^{13}C$ and $\delta^{18}O$ based on replicate analysis of two standards (GBW 04416, GBW 04417). The same powdered samples (~ 50 mg) for bulk-limestone stable isotopic composition were digested in HNO_3 and HF under high temperature (190°C), and diluted to ~ 100 g using 2% HNO_3. For dolomite and calcite mixed samples, to exclude the influence of siliciclastics, the powder (~ 50 mg) digestion was carried out using 3 ml 1mol/L acetic acid at 25°C for 12 hours. The diluted solution was introduced into an Agilent 7700X quadropole inductively coupled plasma mass spectrometer (ICP-MS) for Sr, Mn, and rare earth elements and yttrium (REE+Y) analyses. Appropriate oxide interference corrections were applied running a tuning solution (1.0 ng mL^{-1} of Ce, Co, Li, Mg, Tl and Y, $CeO^+/Ce^+ < 0.3\%$) before calibration.

Dolomite and fossil shells from the polished samples used for BSE images were analyzed for Ca, Mg, Fe, Mn, and Sr with a JEOL JXA-8100 Electron Probe Micro Analyzer (EPMA) equipped with four wavelength-dispersive spectrometers (WDS). An accelerating voltage of 15 kV, a beam current of 20 nA and a 5-15 μm focused electron beam were used to analyze the minerals. Data were corrected on-line using a modified ZAF (atomic number, absorption, fluorescence) correction procedure. Element peaks and backgrounds were measured for all elements with counting times of 10 s and 5 s, respectively (except for Mn, these were 20 s and 10 s, respectively). Values obtained from EPMA spot analysis were used for calibration during *in situ* laser ablation analysis of the same dolomite crystals and fossil shells, performed using a Thermo ICAP-Q ICP-MS. Each laser spot was analyzed for 50 different elements, including the minor, trace, and REE+Y. Rare earth element concentrations were normalized to the Post Archean Australian Shales (PAAS, McLennan, 1989) and then plotted on a logarithmic scale against their atomic numbers to determine the REY distribution patterns.

5. RESULTS

5.1 Bed 24

Bed 24 (71 cm thick), the topmost unit of the Changhsing Formation, is formed of skeletal packstones that are composed of micrite, bioclasts, and cavities. Despite minor variations in the sedimentary texture, Bed 24 is formed, on average, of 23% micrite, 70% skeletal grains, 2% cavity, and 5% unidentified particles (data calculated from Chen et al., 2015, their Table 3). The skeletal grains were derived largely from foraminiferas (17%), brachiopods (12%), and crinoids (11%) along with fewer sponge spicules, ostracods, echinoids, bryozoans, gastropods, algae, and calcareous sponges (Chen et al., 2015).

5.2 Beds 25-62

Excluding the beds formed of claystone (e.g., Beds 25, 26, 28, 32, 37, 48), Beds 27 to 62 are composed of calcareous mudstone and/or skeletal mudstones with an average of 83% micrite and 8% unidentified particles (Chen et al., 2015). The amount and diversity of skeletal grains are much lower than in Bed 24, with only scattered foraminiferas, ostracods, echinoids, and brachiopods being present.

Bed 27, the boundary carbonate, is divided into layers I to VI in ascending order (Fig. 5), based on variations in color, bioturbation intensity, firmground surfaces, and stratigraphic relationship (Zheng et al., 2013; Chen et al., 2015). The bottom of Layer IV is equivalent to the PTB as defined by Yin et al. (2001).

5.3 Mineralogy

Samples from Bed 24 comprise of 95% calcite and 5% quartz (Fig. 4). The claystones in Beds 25 and 26 are formed primarily of illite (~ 60%) and gypsum (~ 30%) with minor amounts of quartz and calcite, whereas the claystones in Bed 28 are formed largely of calcite (~ 65%) and illite (~ 25%) with minor gypsum (Fig. 4).

Samples from Beds 27 to 62 are formed largely of carbonate minerals (25% to 65% calcite and dolomite), quartz (20 – 40%), and phyllosilicates (10 – 40% illite and chlorite) with traces of K-feldspars and pyrite (Fig. 4).

Most of the dolomite is non-ferroan dolomite with less than 5 mol % $FeCO_3$, whereas all the calcite is ferroan. Elemental analyses of dolomite crystals by EPMA indicate that both HCD and LCD are present.

5.4 Diagenetic fabrics

5.4.1 Dolomitization

The allochem grains were rarely replaced by dolomite, whereas the fine matrices were preferentially replaced by dolomite to variable degrees (Fig. 4). The dolomite crystals, 20 − 30 μm long, are present as scattered subhedral to euhedral rhombs, with no stratigraphic pattern to the variance in crystal size. Using the terminology of Sibley and Gregg (1987), the dolomite crystals are characterized by planar boundaries (Fig. 6).

The dolomite crystals are formed of solid crystals and rare hollow crystals. Despite their small size, BSE imaging shows that the dolomite crystals have cores that are separated from the zoned cortices by internal discontinuities (Fig. 6). EMP analysis show that the zones highlighted by BSE imaging are defined by variations in the %Ca content and Fe content of the dolomite (Figs. 6, 7).

The cores of the dolomite crystals, generally < 15 μm long, have an irregular outline (Figs. 6, 7). Despite their irregular outline, an underlying euhedral, rhombic crystal motif is still apparent (Fig. 7). These cores are commonly formed of LCD with many including small (< 3 μm long) pores (Fig.6D-F). In rare examples, the LCD cores contain small (< 5 μm long) calcite inclusions (Fig. 6A). Ferroan LCD cores are rare (Fig. 7A).

The cortices of the dolomite crystals are formed of calcite, HCD, and ferroan HCD zones. The calcite zones have a highly irregular outline characterized by numerous angular reentrants and rounded embayments (Figs. 6,7). Despite the irregular LCD cores and irregular calcite zones, the HCD zones have a rhombic motif (Fig. 6). In some cases, the euhedral HCD zones are encased by overgrowths of ferroan HCD (Fig. 6D-F). The overgrowth is thin (generally < 5 μm) and does not change the shape of euhedral dolomite crystals.

The hollow dolomite crystals have walls, formed of HCD, that are < 10 μm thick and have projections that extend from the inner surfaces into the cavity (Fig.

8A-C). The projections appear to be prismatic calcite and they may represent precipitation that followed dissolution.

5.4.2 Calcitization

Generally, the euhedral HCD cortices of the dolomite crystals have been partially calcitized, with the zoned internal architecture of the dolomite being evident in BSE images. In Layer I of Bed 27, however, the HCD cortices in the dolomite crystals have been almost completely calcitized (Figs. 7C, 8D-F).

5.4.3 Firmground

Firmgrounds are common in Bed 27. They are typically associated with the dark grey lithoclasts, which are constrained at the top of the firmgrounds and extensively bioturbated (Fig. 5), with *Planolites*, *Glossifungites*, and *Thalassinoides* being readily apparent (cf. Zheng et al., 2013; Chen et al., 2015). The burrow systems remained open after the trace maker left, permitting sediments from subsequent depositional events to fill them (Chen et al., 2015). From Layer II to Layer V, the lithoclasts vary from large (up to 2 cm) and rounded shape to small and irregular, which is accompanied by the increasing intensity and diameters of burrows (Fig. 5). The dark lithoclasts are formed of argillaceous limestones, whereas the burrow fillings are formed of argillaceous dolostones and light gray in color, making them distinguished from the lithoclasts.

5.4.4 Cementation

Calcite, largely micrite in size, is the dominant cement, bridging the gaps between the allochem grains (Fig. 9A). In Bed 24, silica is the main cement (Fig. 9B).

5.4.5 Replacement

In Bed 24, some of the skeletal grains (e.g., bryozoan, crinoid, foraminfera) are partially or completely silicified (Fig. 9C). Chambers in the bioclasts are filled with calcite (Fig. 9D) and/or chert. The silicified part of skeletal grains resulted in complete obliteration of primary texture of the grains (Fig. 9C, D).

5.4.6 Recrystallization and dissolution

The calcite crystals between the allochem grains have been recrystallized to various degrees (Fig. 9E). Scattered moldic porosity (Fig. 9F) is present in Bed 24.

5.5 Distribution of diagenetic fabrics

Cementation, silicification, calcite fillings, and recrystallization are common in Bed 24. Beds 25 to 62, however, are characterized by transformation of clay minerals, dolomitization, and calcitization. Layer 27-I underwent complete calcitization.

5.6 Cathodoluminescence

The skeletal grain shells have been altered to variable degrees, displaying cathodoluminescence (CL) ranging from non-luminescence to dull-dull reddish to orange-bright orange (Fig. 10). The silicified shells are non-luminescent.

The dolomite crystals are characterized by zoned CL luminescence. The euhedral HCD zones display bright orange luminescence, the irregular calcite zone display dull-orange luminescence, and the LCD cores are non-luminescent. Bright-orange luminescence characterizes the euhedral calcite crystals that mimic the dolomite rhombs. The lithoclasts and the fine groundmass surrounding the dolomite crystals have dull reddish CL.

The groundmass in Bed 24 displays non-luminescence to dull-orange luminescence (Fig. 10E, F).

5.7 Stable isotope composition

Calcite from Bed 24 has $\delta^{13}C$ values from 1.72 to 2.92‰, and $\delta^{18}O$ values from −7.74 to −4.84‰. In claystone beds 26 and 28, the calcite has $\delta^{13}C$ values of −0.77‰ and −0.76‰, and $\delta^{18}O$ values of −7.82 to −7.78‰, respectively. In Beds 27 to 62, separate analysis of the dolomite and calcite indicates that the $\delta^{13}C$ and $\delta^{18}O$ values of calcite range from −1.52‰ to 2.05‰, and from −10.24‰ to −3.33‰, respectively. In contrast, the $\delta^{13}C$ and $\delta^{18}O$ values of the coexisting dolomite ranges from -1.47‰ to 4.11‰, and from −7.38‰ to −1.79‰, respectively. The $\delta^{13}C$ and $\delta^{18}O$ values of bulk carbonates from Beds 27 and 62 range from -0.76‰ to 1.28‰, and from -8.58‰ to -3.99‰, respectively. A positive correlation exists between the $\delta^{13}C$ and $\delta^{18}O$ values for calcite and dolomite from beds 27 to 62 (r = 0.6; Fig. 11). The bulk carbonates display similar stratigraphic trend of $\delta^{13}C$ and $\delta^{18}O$ values to the calcite (Fig. 4). The stratigraphic trend of differences in $\delta^{13}C$ between dolomite and calcite ($\Delta\delta^{13}C_{dol\text{-}cc}$) is similar to that of $\delta^{13}C$ for dolomite (Fig. 4). For bulk carbonate samples from Beds 27 to 62, positive correlations exist between the $\delta^{13}C$ values and dolomite content (r = 0.6, Fig. 12), and between the $\delta^{18}O$ values and dolomite content (r = 0.8, Fig. 12).

5.8 Minor and trace elements

Bulk samples from Bed 24 yielded Sr concentrations of 404 to 857 ppm (average 590 ppm, n = 9), Mn concentrations 118 to 475 ppm (average 240 ppm, n = 9), and the Mn/Sr ratios are normally < 1. A negative correlation exists between Sr and Mn for bulk samples from Bed 24 (r = 0.6, Fig. 12).

In the Yinkeng Formation, the Sr content of the brachiopod shells varies between 746 and 837 ppm (average 780 ppm), whereas the Sr in the dolomite is generally less than 300 ppm. The Mn and Fe contents in the brachiopod shells vary from 368 to 462 ppm, and from 855 to 1050 ppm, respectively, which are depleted, if compared to the dolomite crystals. The bulk carbonate minerals from Beds 27 to 62 yielded Sr concentrations of 73 to 909 ppm (average 184 ppm, n = 33), Mn concentrations 228 to 2180 ppm (average 678 ppm, n = 33), and the Mn/Sr ratios range from 0.8 to 12.7 (average 4.5, n = 33). Poor correlations exist between Mn and Sr, and between Sr and dolomite content, whereas relatively strong correlations exist between the Sr and clay mineral content, and between the Mn and dolomite content are (Fig. 12). The stable isotopic compositions of bulk carbonate minerals from Beds 27 to 62 display no correlation with Mn/Sr (Fig. 12).

5.9 ΣREE+Y

In Bed 24, the ΣREE and Y of the bulk rock samples range from 8.0 to 55.1 ppm (average 23.4 ppm), and from 2.0 to 11.9 ppm (average 5.5 ppm), respectively. For brachiopod shells, the ΣREE and Y values ranges from 56.2 to 71.3 ppm (average 63.4 ppm), and from 8.2 to 11.5 ppm (average 9.9 ppm), respectively. The dolomite samples have higher ΣREE and Y values (ΣREE is ~ 93.1 ppm, Y is 25.9 ppm).

The shale-normalized REY distribution patterns (Fig. 13) of samples from Beds 24 to 62 are characterized by the following features.

a) The shells display heavy REE (HREE) depletion (average Dy_{SN}/Sm_{SN} = 0.6, n = 4), whereas the bulk samples of Bed 24 (average Dy_{SN}/Sm_{SN} = 1.3, n = 9) and dolomite crystals (average Dy_{SN}/Sm_{SN} = 1.0, n = 4) all display HREE enrichment.

b) The shells have the lowest La_{SN}/Nd_{SN} ratios (La_{SN}/Sm_{SN} = 0.5-0.6), dolomite is intermediate (La_{SN}/Sm_{SN} = 0.6-0.8), and the bulk sample from Bed 24 has the highest ratio (La_{SN}/Sm_{SN} = 0.8-1.1).

c) All the samples display true negative Ce anomalies represented by negative Ce/Ce* (0.7-0.9, average is 0.8, n = 17) and positive Pr/Pr* (1.0-1.2, average is 1.1, n = 17) values.

d) The superchondritic Y/Ho molar ratios for all the samples range from 2.1 to 2.8.

e) All the samples display negative Eu anomaly (Eu/Eu*, $Eu^* = 0.5 \times Sm_{SN} + 0.5 \times Gd_{SN}$) except one dolomite sample (Eu/Eu* = 1.1).

6. INTERPRETATION

6.1 Mineralogy

Compared to the uppermost bed in the Changhsing Formation (i.e., Bed 24), Beds 25 to 62 display a significant increase in quartz (from ≤5% to 25−30%), clay minerals (from 0 to 10−40%), and dolomite (from 0 to 0−50%). The dramatic siliciclastic input in Beds 25 to 62 as opposed to Bed 24 suggests that an intense and stable supply source of terrigenous sediments existed during the deposition of these beds. This suggestion is consistent with the finding that the seawater $^{87}Sr/^{86}Sr$ ratios display a rapid increase starting from Bed 25 of the Meishan section to the middle-late Spathian (Song et al., 2015). The terrigenous sediments may have been transported across the carbonate platform from the adjacent landmass or supplied axially into the basin. The siliciclastic input was probably derived from the Huaxia Old-land, which was ~ 200 km southeast of Meishan during the Early Triassic (Feng et al., 1997). Another possible source is volcanic ash released by Siberian Trap volcanism that was active during the Permian-Triassic transitional period (Korte and Kozur, 2010; Brand et al., 2012).

Compared to the amount of quartz in Beds 27 to 62, the quartz content in the claystone beds (e.g., Beds 25, 26, and 28) is almost negligible, which may have been related to the rates of sea-level change and the source of clastic sediments. Beds 25 and 26 represent starved deposits in a shelf margin system tract (SMST), whereas Bed 27 and higher beds were deposited slowly in a transgressive system tract (TST) (Zhang et al., 1997). It has been argued that the clay minerals (dominantly illite) in the claystones probably resulted from the marine diagenesis of smectite that came from the land and volcanic ash (He, 1989; Hong et al., 2008). If this is true, the smectite implies that deposition of the claystone beds probably took place under a semi-arid climate because that is favorable for smectite formation (Worden and Morad, 2003). The presence of gypsum (25 − 30 wt.%) in these clay beds supports this assessment.

6.2 Diagenetic fabrics

Diagenetic fabrics in Beds 24 to 62 include evidence of alteration that took place in the marine, the meteoric, and burial environments. Marine diagenetic fabrics include (1) firmgrounds (James and Bone, 1992; Nicolaides and Wallace, 1997; Melim et al., 2004; Gruszczynski et al., 2008), (2) syndepositional dolomitization (Schauer and Aigner, 1997; Yoo and Lee, 1998; Torok, 2000; Swart et al., 2005; Zentmyer et al., 2011), (3) incorporation of micrite as cement, and (4) silicification of skeletal grains ascribed to remobilization of unstable opaline silica derived from sponge spicules (Scholle, 1971; Jacka, 1974; Mu and Riding, 1988).

Meteoric diagenesis involved calcitization of dolomite crystals (Jones et al., 1989; James et al., 1993; Purser et al., 1994; Kyser et al., 2002; Scholle and Ulmer-Scholle, 2003; Jones, 2007). As noted by James et al. (1993) and Kyser et al. (2002), dissolution driven by reaction between meteoric groundwater and Ca-rich dolomites removed the cores of many crystals, leaving an irregular void that was subsequently filled with calcite.

Burial diagenetic fabrics include (1) development of ferroan-dolomite cortices (McHargue and Price, 1982), and (2) formation of uniform illite-chlorite assemblage at the expense of smectite and chlorite (Muller, 1967; Scholle, 1971).

6.3 Stable isotopes

Korte et al. (2005a) reported $\delta^{18}O$ and $\delta^{13}C$ values of unaltered brachiopods from the latest Permian in Italy to be −4.03‰ and 0.86‰, respectively. The oxygen isotopes of Late Permian brachiopods from the Tethys region are somewhat depleted relative to their counterparts from Russia (−0.75 to 1.48‰, from Popp et al., 1986) and Norway (−4.0 to −2.2‰, from Mii et al., 1997). Considering the normal poleward decline in temperatures, the lower oxygen isotope values at equatorial Tethys, if compared to the polar Russia and Norway, are expected. Hence, the values reported by Korte et al. (2005a) can be treated as reliable data to represent the stable isotopic compositions of the primary low Mg-calcite (LMC) precipitated from Upper Permian seawater, given that the primary mineralogy of brachiopod shells is LMC and that no vital effect exists for brachiopods (Lowenstam, 1961; Lee and Wan, 2000). Reliable $\delta^{18}O$ and $\delta^{13}C$ values of unaltered carbonate rocks and brachiopods, however, are not available for the earliest Triassic (Korte et al., 2005b).

Compared to the primary LMC, the diagenetic LMC (d-LMC) in Bed 24 displays dramatic depletion in $\delta^{18}O$ (~1 − 4‰ lower), indicating diagenetic alteration of Bed 24 after its deposition. The negative shift in $\delta^{18}O$ values can be ascribed to (1) alteration by subaerial meteoric diagenesis, and/or (2) recrystallization in the burial process under elevated temperatures. Both options are viable, given that scattered moldic porosity (Fig. 9F) and calcite recrystallization (Fig. 9E) are found in samples from Bed 24. Given the large variation in $\delta^{18}O$ values (~ 3‰) but relatively consistent $\delta^{13}C$ values, the diagenetic alteration probably took place in a relatively closed environment with low water/rock ratio. Compared to Bed 24, the $\delta^{18}O$ values of d-LMC in Beds 25 to 62 are ~ 1‰ lower, indicating a higher degree of diagenetic alteration. The negative shift in $\delta^{18}O$ values of Beds 25 to 62, however, is ascribed to meteoric diagenesis, given the widespread calcitization of the dolomite and positive correlation between the $\delta^{18}O$ and $\delta^{13}C$ values in the calcite (Fig. 11). For samples with mixed dolomite and calcite, the positive correlations between stable isotopic compositions and dolomite content (Fig. 12) indicate that the isotopic compositions are altered by dolomitization.

The $\delta^{18}O$ values of dolomite in Beds 27 to 62 are similar to the reported oxygen isotope composition of Griesbachian whole rocks (assumed to be formed of dolomite) from Palazzo, Sicily, which range from -2.67 to -1.82‰ (Korte et al., 2005b). They are, however, significantly depleted in ^{18}O if compared to modern dolomites that formed from marine or hypersaline or mixed marine and/or meteoric waters (Major et al., 1992; Budd, 1997; Compton et al., 2001). It reflects the fact that the replacement dolomites must have been significantly modified after their initial formation (Spötl and Burns, 1991). For calcite and coexisting dolomite, the difference in $\delta^{18}O$ values is probably caused by the differential mineralogic fractionation between dolomite and calcite (Degens and Epstein, 1964; Veizer and Hoefs, 1976; Land, 1980; Gao, 1993; Kah, 2000; Vasconcelos et al., 2005).

6.4 Minor and trace elements

Bulk limestones from Bed 24 display higher Sr but lower Mn concentrations than the bulk carbonates from Beds 27 to 62 (Fig. 12), implying stronger diagenetic alteration of the latter samples. The latter samples also have higher Mn/Sr ratios and large variation of Mn/Sr ratios (Fig. 12), suggesting diagenetic alteration (such as dolomitization) of various degrees.

Compared to brachiopod shells, the dolomites in Beds 27 to 62 have higher Mn and Fe contents, indicating dolomitization processes and/or the modification of dolomites in a reduced environment. The low Sr concentration (< 300 ppm) combined with negatively shifted $\delta^{18}O$ values of dolomite suggest diagenetic modification after their formation (Spötl and Burns, 1991; Huebscher, 1996; Yoo and Lee, 1998). Given that meteoric water is commonly depleted in $\delta^{18}O$, dolomite recrystallization in a setting where meteoric infiltration lasted a long time and/or took place at slightly elevated temperatures during shallow burial is considered to be the most plausible mechanism for progressive modification.

6.5 ΣREE+Y

The samples in Bed 24 display modern seawater-like shale-normalized REE + Y (REY) patterns (Fig. 13), which is characterized by (1) enrichment of HREE relative to light REE (LREE), (2) negative Ce anomalies (Ce/Ce* < 1), (3) positive La anomalies, and (4) high Y/Ho ratios (Bau and Dulski, 1996; Shields and Webb, 2004). Hence, the seawater from which the Bed 24 was deposited was akin to the modern oxygenated seawater.

For dolomites in Beds 27 to 62, the "MREE-bulge" of PAAS-normalized REY patterns (Fig. 13) probably indicates fully anoxic conditions of dolomitization process and/or modification of dolomite, given that the scavenged MREE in Fe oxides in the water column were released in fully anoxic condition (Haley et al., 2004; Corlett and Jones, 2012).

For brachiopod shells, their PAAS-normalized REY patterns show LREE enrichment relative to HREE (Fig. 13), which could be ascribed to (1) the direct contamination of shells by materials (such as shale) that were heavily enriched in LREE (Wray, 1995; Nothdurft et al., 2004), or (2) the precipitation of shells from seawater with different REY property from where Bed 24 was deposited. The first option is discounted, because the mixture of shale and marine carbonate would not produce LREE enrichment (Nothdurft et al., 2004, their Figure 4). During the earliest Triassic, the Meishan locality was separated from the continental coast by a carbonate platform (Feng et al., 1997). Therefore, despite the LREE-enriched pattern of the suspended load from modern river water (Goldstein and Jacobsen, 1988), the inclusion of LREE-enriched estuarine particulate and/or colloidal in brachiopod shells precipitated from LREE-depleted seawater is not reasonable. The LREE associated with particulate organic matter in the water column, however, are released in oxic to suboxic conditions at the sediment water interface (Sholkovitz et al., 1994). Hence, the LREE enrichment in the shells probably results from their deposition across the oxic-suboxic boundary.

7. DISCUSSION

7.1 Diagenetic conditions in PTB intervals

The PAAS-normalized REY patterns of brachiopod shells (Fig. 13) indicate that the depositional conditions for the formation of Beds 25 to 62 were not fully anoxic. Fully anoxic conditions, however, are required to account for the MREE bulge pattern in the dolomite. Therefore, the dolomite crystals, if syndepositional in origin, must have been modified after their initial formation. The zoned internal architectures of the dolomite crystals indicate that they either form episodically (Kyser et al., 2002) or they formed continuously from a fluid that changed its composition with time (Jones and Luth, 2002). In this case, the zones are distinguished from each other by compositional and luminescent zoning. The variation from a bright-orange HCD cortical zone to a dull-orange calcite cortical zone to a non-luminescent LCD core reflects the multiple-stage dolomitization and/or dolomite modification, which operated with fluids of different chemical compositions and/or under different redox conditions.

The HCD cortical zone is syndepositional to early diagenetic in origin (Fig. 14), given its formation of euhedral and fine dolomite crystal with a high $CaCO_3$ content. The euhedral HCD crystals replaced carbonate mud but preserved the original rock texture (Figs. 6-8), which is similar to the widely reported feature of syndepositional dolomite in carbonate sediments deposited in ramp depositional environment (Schauer and Aigner, 1997; Yoo and Lee, 1998; Torok, 2000; Swart et al., 2005; Zentmyer et al., 2011).

The HCD cortical zone displays a discontinuity with an inner irregular calcite zone (Fig. 6). The discontinuities typically imply dissolution of cores and subsequent filling with calcite or dolomite (James et al., 1993; Torok, 2000; Kyser et al., 2002; Jones, 2005, 2007). The preferential dissolution of dolomite cores is typically attributed to the higher solubility of cores than the crystal rims, which is linked to the higher $CaCO_3$ content and higher density of growth defects in the cores (Jones, 2007). The calcitization of dolomite crystals have been reported from various diagenetic environments, including fresh meteoric water (Longman and Mench, 1978; Lee and Harwood, 1989; James et al., 1993; Kyser et al., 2002), mixing marine and meteoric waters (Magaritz and Kafri, 1981), and burial hot brine (Land and Prezbindowski, 1981). In the Meishan section, several lines of evidence, however, indicate that the early-formed HCD were probably calcitized during sea-level lowstands through infiltration of meteoric fluids into the syndepositional dolomites. First, the maximum calcitization of euhedral HCD crystals occurred in Layer 27-I, which overlies the Beds 25 and 26 composed of claystones with 25-30 wt.% gypsum (Fig. 4). Some gypsum crystals display dissolved surfaces (Yin et al., 1994). In the Xiushui section

(South China), which was deposited on Yangtze carbonate platform, the stratigraphic unit equivalent to Layer 27-I is lost, but the Beds 2 and 3, which are equivalent to Bed 26 in the Meishan section, display meteoric diagenetic features (Wu et al., 2014). A subaerial exposure surface, characterized by reddish limonite coating on skeletal grains, is present at the top of Bed 2, whereas dedolomitization is prevalent in Bed 3 (Wu et al., 2014). The dedolomitization is ascribed to the meteoric alteration associated with the end-Permian sea-level regression (Wu et al., 2014). Given the substantial sea-level drop at the end of Permian (Newell, 1967; Holser and Magaritz, 1987; Yin et al., 2014) but the preservation of continuous conodont zone in Meishan section, it can be postulated that the dedolomitization of intervals above Bed 26 was probably caused by meteoric alteration during the short-lived subaerial exposure of intervals in sea-level regressions. Secondly, the $\delta^{18}O$ value of the Layer 27-I is the minimum (-8.09‰) in this study, which is consistent with the finding that the maximum meteoric alteration occurred in Layer 27-I. Finally, despite the Fe-rich nature of the calcite (i.e. dedolomite), its dull-orange to bright-orange luminescence suggests enrichment of Mn in meteoric diagenesis (Popp, 1986).

Given the rhombic motif of the LCD core and its presence in calcite cortice (Figs. 6, 7), the LCD core is probably re-dolomitization of the calcite cortice (Fig. 14) when meteoric fluids were replaced/modified by seawater during subsequent sea-level highstands and/or shallow burial process. The non-luminescence nature of LCD cores indicates the enrichment of Fe from reduced fluids, as substantiated by the rare presence of Fe-LCD (Fig. 7A).

The outmost iron-rich HCD zone suggests shallow burial modification, due to the fact that (1) its growth does not change the euhedral crystal shape of HCD cortice, (2) the ferroan composition of the outmost zone (Scholle, 1971). The clay minerals in embayed ferroan HCD zone probably suggest growth of ferroan HCD in consumption of Mg released during burial transformation of clay minerals (McHargue and Price, 1982).

7.2 Comparison the Meishan section with other PTB sections

Bulk sample analysis of the global PTB intervals indicates a negative shift in $\delta^{13}C$ from the late Changhsingian *Clarkina yini* Zone to the early Griesbachian *Isarcicella isarcica* Zone, with two minimum peaks being present at the extinction horizon and *H. parvus* Zone to *Isarcicella isarcica* Zone (Fig.1; Kearsey et al., 2009; Korte and Kozur, 2010; Song et al., 2013; Yin et al., 2014). Whether or not the globally synchronistic negative shift in $\delta^{13}C$ across the PTB was altered by diagenesis is still open to debate. Most studies have argued, without solid petrographic data, that the $\delta^{13}C$ values have not been affected by diagenesis, given (1) the non-existence of positive covariation between $\delta^{13}C$ and $\delta^{18}O$ (Korte et al., 2004; Horacek et al., 2007; Song et al., 2013), (2) the $\delta^{18}O$ values being between −4‰ and −8‰ for most samples (Fig. 15), which are not indicative of extensive dissolution-precipitation (Song et al., 2013), and (3) the low Mn/Sr ratios (< 10) (Song et al., 2013). Heydari et al. (2001) suggested, however, based on whole rock isotopic compositions of PTB intervals from China, Italy, Austria, and Iran, that the stable $\delta^{13}C$ and $\delta^{18}O$ have been altered by meteoric diagenesis. Despite the $\delta^{18}O$ values being between −4‰ and −8‰, widespread meteoric diagenetic alteration were reported in Pleistocene carbonates (Braithwaite and Montaggioni, 2009; Swart and Kennedy, 2012; Li and Jones, 2013; Oehlert and Swart, 2014). Similarly, despite the low Mn/Sr ratios (< 1), the presence of dolomite and high Mn concentration (> 400 ppm) combined with positive correlation between $\delta^{13}C$ and $\delta^{18}O$ indicate that the negative $\delta^{13}C$ anomaly is not primary in origin (Derry, 2010).

Separate analyses of the calcite and dolomite carbon isotopes in the Meishan section indicate that the dramatic negative shift in $\delta^{13}C$ occurs in the calcite from claystone beds 26 (*H. changxingensis* Zone) and 28 (*I. staeschei* Zone). The calcite in the claystone beds have an average $\delta^{18}O$ value of -7.80‰, which is similar to the $\delta^{18}O$ values of calcites from Layer 27-I (-8.09‰). Given that the calcite in Layer 27-I resulted from calcitization of euhedral HCD crystals in a meteoric diagenetic environment, the similar $\delta^{18}O$ value of calcite in claystone beds are probably meteoric in origin. The negative $\delta^{13}C$ values of calcite in beds 26 and 28 probably originated from incorporation of more ^{12}C from the subaerial vadose zone. Therefore, the two peaks of negative shift in the $\delta^{13}C$ in the PTB interval are probably related to modification in subaerial exposure conditions associated with the sea-level regressions. Taking the first $\delta^{13}C$ minimum as an example, the similar position of $\delta^{13}C$ excursions relative to the extinction horizon implies that the topmost Permian beds were subaerially exposed at or near the extinction horizon. The fact that the shallow marine PTB sections (e.g., Val Brutta) in the southern Alps display dramatic negative shift in both the $\delta^{18}O$ and $\delta^{13}C$ isotope record near the extinction horizon (Kearsey et al., 2009) is consistent with the assertion of subaerial diagenesis. End-Permian regression was also verified to take place in the whole South China during the *C. meishanensis* zone and *H. changxingensis* zone (Yin et al., 2014). The topmost Permian strata in Nanpanjiang basin experienced one and possibly two small-scale relative sea-level changes prior to the Early Triassic transgression (Collin et al., 2009; Hallam and Wignall, 1999). Subaerial vadose features, including paleosol (Hallam and Wignall, 1999), geopetal sediments, etched grains, and pendent and meniscus cements, developed before the extinction horizon and were truncated by subsequent erosion of the final Permian surface (Collin et al., 2009).

Extensive dolomitization has been reported in the PTB intervals (Collin et al., 2009; Kearsey et al., 2009; Cao et al., 2010; Jiang et al., 2014). It is generally assumed that limestones with a higher dolomite content will have a higher $\delta^{18}O$ bulk rock isotope value (usually > −4‰) (Fig. 15; Horacek et al., 2007), but the carbon isotope values are not significantly altered by diagenesis, as the carbon reservoir in the rock is thought to be greater than that in the diagenetic fluid (Horacek et al., 2007; Algeo et al., 2007). Indeed, the large variation in $\delta^{18}O$ values but relatively consistent $\delta^{13}C$ values for samples from Beds 27 to 62 (Fig. 11) indicates that the diagenetic alteration probably took place in a relatively closed environment with low water/rock ratio. The $\delta^{13}C$ composition of marine carbonates, however, could be substantially altered when large quantities of organic matter or methane have been oxidized (Irwin et al., 1977; Schobben et al., 2016). In the dolomite-bearing beds in the Meishan section, the $\delta^{13}C$ values of calcite is ~ 1.7‰ (σ = 0.7‰, n = 39) lower than that of the coexisting dolomite (Figs. 4, 11; Table 1), which is common between dolomites mediated by sulfate-reducing bacteria (SRB) and their surrounding calcite matrices (Gingras et al., 2004; Corlett and Jones, 2012; Baniak et al., 2013, 2014). Given that the outmost Fe-HCD cortical zone is formed in reducing condition, which is compatible for the mediation by SRB, the ferroan HCD zone is probably product of SRB mediation. Petrographic evidence shows that the ferroan HCD zones display intercalation with clay minerals, suggesting the formation of ferroan HCD associated with clay minerals. Given the introduced Mg-rich smectite after the Permian-Triassic mass extinction event (PTME), likely due to volcanic ashes related to the Siberian Trap volcanism (Korte and Kozur, 2010; Brand et al., 2012), the transformation of smectite into illite during the burial stage provides Mg for dolomitization.

As suggested by Macouin et al. (2012), the similar trends between $\Delta^{13}C_{carb-org}$ and $\delta^{13}C_{carb}$ is also a feature of dolomitization involving SRB. Indeed, the $\Delta^{13}C_{carb-org}$ and $\delta^{13}C_{carb}$ from Beds 27 to 40 in Meishan section display similar trend (Huang et al., 2007; Luo et al., 2011). The PTB intervals from Abadeh section, Iran show the same case (Korte al., 2004). In the Meishan section, the total organic carbon (TOC) values are low in Beds 27 and 28, but relatively high in Beds 24 to 26 (Yin et al., 2012). The available organic matter in sediments can be used by SRB to produce H_2S and iron sulphide and/or iron monosulphide (Taylor and Sibley, 1986; Macouin et al., 2012). In Meishan section, the beds with high TOC usually display more amount of pyrite framboids (Yin et al., 2012). The remaining Fe^{2+} was available for the formation of ferroan dolomite (Taylor and Sibley, 1986). Due to the involvement of SRB in the microbial mediation, the precipitated calcite display more negative values due to incorporation of ^{12}C. Additionally, sulfate is a well-known inhibitor for the nucleation and continuous growth of dolomite. The substantial drawdown of seawater sulfate in early Triassic (Song et al., 2014), however, should facilitate the formation of dolomite (Vasconcelos et al., 1995; Vasconcelos and McKenzie, 1997).

The $\delta^{13}C_{carb}$ compositions of bulk rock samples from global PTB sections indicate that the PTB intervals formed in deep water (> 200 m) have much lower $\delta^{13}C_{carb}$ values than the intervals formed in shallower water (Fig. 15). Considering that both organic matter and clay minerals play important roles in SRB mediated dolomitization, the relatively more positive $\delta^{13}C_{carb}$ values of shallower water sediments could be ascribed to the less formation of ferroan dolomite mediated by SRB, given (1) the oxidation of organic matter during subaerial exposure of sediments after their deposition, and (2) less preservation of clay minerals due to relatively higher energy of depositional environment compared to basinal environment.

CONCLUSIONS

Examination of the diagenetic features across the Permian-Triassic boundary from Meishan section has demonstrated the following points.

(1) The dolomite crystals show zoned internal architecture, including an irregular non-luminescent LCD core which is encased successively by an irregular dull-orange luminescent calcite zone, an inner bright-orange luminescent HCD cortex, and the outmost ferroan-HCD cortex.

(2) The dolomite crystals underwent diagenetic modifications after their syndepositional formation. The modifications include calcitization by meteoric water, re-dolomitization of calcite, and overgrowth of ferroan dolomite in burial process.

(3) The dramatic negative $\delta^{13}C$ excursions in Beds 26 and 28 are related to meteoric diagenesis, whereas in dolomite-bearing beds, the lower $\delta^{13}C$ values of calcite than coexisting dolomite are caused by biologically mediated dolomitization in burial process.

The diagenesis in carbonate succession across PTB does change the primary $\delta^{13}C$. The negative shift in $\delta^{13}C$ values of calcite in claystone beds is caused by meteoric diagenesis, while the burial dolomitization contributes to ~ 1.7‰ negative shift in $\delta^{13}C$ of coexisting calcite. Hence, diagenesis has to be taken into consideration to explain the synchronistic $\delta^{13}C$ excursions.

ACKNOWLEDGEMENT

The research was supported by the National Natural Science Foundation of China (Grant 41502103), Natural Science Foundation of Hubei Province (Grant 2015CFB360), Scientific Research Foundation for Returned Scholars, Ministry of Education of China (Grant KZ15Z20057), Fundamental Research Funds for the

Central Universities (G1323531529, CUGL150835), and the State Key Lab of Biogeology and Environmental Geology (GKZ15Y670). I am grateful to Dr. K. Muehlenbachs, University of Alberta, who ran the stable isotope analysis in his Stable Isotope Laboratory; the State Key Laboratory of Geological Processes and Mineral Resources (GPMR), who provide the laboratories for XRD, EPMA, LA-ICPMS, and SEM analyses; the State Key Laboratory of Biogeology and Environmental Geology, who provide the laboratories for CL observation and solution ICPMS analysis; Drs. Haijun Song and Huyue Song who provide access to samples; and Drs. Li Tian and Mao Luo who assisted the field work to collect samples. I am also greatly indebted to Dr. Brian Jones for his countless hours of editing the paper.

REFERENCE

Algeo, T.J., Ellwood, B., Nguyen, T.K.T., Rowe, H., Maynard, J.B., 2007. The Permian-Triassic boundary at Nhi Tao, Vietnam: Evidence for recurrent influx of sulfidic watermasses to a shallow-marine carbonate platform. Palaeogeography Palaeoclimatology Palaeoecology 252, 304-327.

Allan, J.R., Matthews, R.K., 1982. Isotope signatures associated with early meteoric diagenesis. Sedimentology 29, 797-817.

Baniak, G.M., Amskold, L., Konhauser, K.O., Muehlenbachs, K., Pemberton, S.G., Gingras, M.K., 2014. Sabkha and burrow-mediated dolomitization in the Mississippian Debolt Formation, Northwestern Alberta, Canada. Ichnos 21, 158-174.

Baniak, G.M., Gingras, M.K., Pemberton, S.G., 2013. Reservoir characterization of burrow-associated dolomites in the Upper Devonian Wabamun Group, Pine Creek gas field, central Alberta, Canada. Marine and Petroleum Geology 48, 275-292.

Bau, M., Dulski, P., 1996. Distribution of yttrium and rare-earth elements in the Penge and Kuruman iron-formations, Transvaal Supergroup, South Africa. Precambrian Research 79, 37-55.

Baud, A., Magaritz, M., Holser, W.T., 1989. Permian-Triassic of the Tethys: Carbon isotope studies. Geologische Rundschau 78, 649-677.

Braithwaite, C.J.R., Montaggioni, L., 2009. The Great Barrier Reef: a 700000 year diagenetic history. Sedimentology 56, 1591-1622.

Brand, U., Posenato, R., Came, R., Affek, H., Angiolini, L., Azmy, K., Farabegoli, E., 2012. The end-Permian mass extinction: a rapid volcanic CO_2 and CH_4-climatic catastrophe. Chemical Geology 322-323, 121-144.

Broglio Loriga, C., Cassinis, G., 1992. The Permo-Triassic boundary in the Southern Alps (Italy) and in adjacent Periadriatic regions. In: W.C. Sweet, Z. Yang, J.M. Dickins, H. Yin (Eds.), Permo-Triassic Events in the Eastern Tethys Stratigraphy Classification and Relations with the Western Tethys. Cambridge University Press, pp. 78-97.

Budd, D.A., 1997. Cenozoic dolomites of carbonate islands: their attributes and origin. Earth-Science Reviews 42, 1-47.

Burgess, S.D., Bowring, S., Shen, S., 2014. High-precision timeline for Earth's most severe extinction. Proceedings of the National Academy of Sciences of the United States of America 111, 3316-3321.

Cao, C., Zheng, Q., 2009. Geological event sequences of the Permian-Triassic transition recorded in the microfacies in Meishan section. Science China-Earth Sciences 52, 1529-1536.

Cao, C., Yang, Y., Shen, S., Wang, W., Zheng, Q., Summons, R.E., 2010. Pattern of $\delta^{13}C_{carb}$ and implications for geological events during the Permian-Triassic transition in South China. Geological Journal 45, 186-194.

Chen, Z., Yang, H., Luo, M., Benton, M.J., Kaiho, K., Zhao, L., Huang, Y., Zhang, K., Fang, Y., Jiang, H., Qiu, H., Li, Y., Tu, C., Shi, L., Zhang, L., Feng, X., Chen, L., 2015. Complete biotic and sedimentary records of the Permian-Triassic transition from Meishan section, South China: Ecologically assessing mass extinction and its aftermath. Earth-Science Reviews 149, 67-107.

Chung, F.H., 1974. Quantitative interpretation of X-ray diffraction patterns of mixtures. I. Matrix-flushing method for quantitative multicomponent analysis. Journal of Applied Crystallography 7, 519-525.

Collin, P., Kershaw, S., Crasquin-Soleau, S., Feng, Q., 2009. Facies changes and diagenetic processes across the Permian-Triassic boundary event horizon, Great Bank of Guizhou, South China: a controversy of erosion and dissolution. Sedimentology 56, 677-693.

Compton, J., Harris, C., Thompson, S., 2001. Pleistocene dolomite from the Namibian shelf: High 87Sr/86Sr and 18O values indicate an evaporative, mixed-water origin. Journal of Sedimentary Research 71, 800-808.

Corlett, H., Jones, B., 2012. Petrographic and geochemical contrasts between calcite and dolomite filled burrows in the Middle Devonian Lonely Bay Formation, Northwest Territories, Canada: implications for dolomite formation in Paleozoic burrows. Journal of Sedimentary Research 82, 648-663.

Degens, E.T., Epstein, S., 1964. Oxygen and carbon isotope ratios in coexisting calcites and dolomites from recent and ancient sediments. Geochimica et Cosmochimica Acta 28, 23-44.

Derry, L.A., 2010. On the significance of 13C correlations in ancient sediments. Earth and Planetary Science Letters 296, 497-501.

Feng, Z., Bao, Z., Li, S., 1997. Lithofacies Paleogeography of Early and Middle

Triassic of South China. Petroleum Industry Press, Beijing, 222 pp. (in Chinese)
Folk, R.L., 1959. Practical petrographic classification of limestones. Bulletin of the American Association of Petroleum Geologists 43, 1-38.
Gao, G., 1993. The temperature and oxygen-isotope composition of early Devonian oceans. Nature 361, 712-714.
Gingras, M.K., Pemberton, S.G., Muehlenbachs, K., Machel, H.G., 2004. Conceptual models for burrow-related, selective dolomitization with textural and isotopic evidence from the Tyndall Stone, Canada. Geobiology 2, 21-30.
Goldstein, S.J., Jacobsen, S.B., 1988. Rare earth elements in river waters. Earth and Planetary Science Letters 89, 35-47.
Gruszczynski, M., Marshall, J.D., Goldring, R., Coleman, M., Malkowski, K., Gazdzicka, E., Semil, J., Gatt, P., 2008. Hiatal surfaces from the Miocene Globigerina Limestone Formation of Malta: Biostratigraphy, sedimentology, trace fossils and early diagenesis. Palaeogeography Palaeoclimatology Palaeoecology 270, 239-251.
Haley, B.A., Klinkhammer, G.P., McManus, J., 2004. Rare earth elements in pore waters of marine sediments. Geochimica et Cosmochimica Acta 68, 1265-1279.
Hallam, A., Wignall, P.B., 1999. Mass extinctions and sea-level changes. Earth-Science Reviews 48, 217-250.
He, J., 1989. Restudy of the Permian-Triassic boundary clay in Meishan, Changxing, Zhejiang, China. Historical Biology: An International Journal of Paleobiology 2, 73-87.
Hermoso, M., Callonnec, L.L., Minoletti, F., Renard, M., Hesselbo, S.P., 2009. Expression of the Early Toarcian negative carbon-isotope excursion in separated carbonate microfractions (Jurassic, Paris Basin). Earth and Planetary Science Letters 277, 194-203.
Heydari, E., Hassandzadeh, J., Wade, W.J., 2000. Geochemistry of central Tethyan Upper Permian and Lower Triassic strata, Abadeh region, Iran. Sedimentary Geology 137, 85-99.
Heydari, E., Wade, W.J., Hassandzadeh, J., 2001. Diagenetic origin of carbon and oxygen isotope compositions of Permian-Triassic boundary strata. Sedimentary Geology 143, 191-197.
Heydari, E., Hassandzadeh, J., Wade, W.J., Ghazi, A.M., 2003. Permian-Triassic

boundary interval in the Abadeh section of Iran with implications for mass extinction: Part I - Sedimentology. Palaeogeography Palaeoclimatology Palaeoecology 193, 405-423.

Holser, W.T., Magaritz, M., 1987. Events near the Permian-Triassic boundary. Modern Geology 11, 155-180.

Holser, W.T., Schonlaub, H., Attrep, M., Boeckelmann, K., Klein, P., Magaritz, M., Orth, C.J., Fenninger, A., Jenny, C., Kralik, M., Mauritsch, H., Pak, E., Schramm, J., Stattegger, K., Schmoller, R., 1989. A unique geochemical record at the Permian/Triassic boundary. Nature 337, 39-44.

Hong, H.L., Zhang, N., Li, Z., Xue, H., Xia, W., Yu, N., 2008. Clay mineralogy across the P-T boundary of the Xiakou section, China: Evidence of clay provenance and environment. Clays and Clay Minerals 56, 131-143.

Horacek, M., Brandner, R., Abart, R., 2007. Carbon isotope record of the P/T boundary and the Lower Triassic in the Southern Alps: Evidence for rapid changes in storage of organic carbon. Palaeogeography Palaeoclimatology Palaeoecology 252, 347-354.

Huang, J., Luo, G., Bai, X., Tang, X., 2007. Organic fraction of the total carbon burial flux deduced from carbon isotopes across the Permo-Triassic boundary at Meishan, Zhejiang Province, China. Frontiers of Earth Science in China 1, 425-430.

Huebscher, H., 1996. Regional controls on the stratigraphic and diagenetic evolution of Woodbend Group Carbonates, North-central Alberta, Canada, University of Alberta, Edmonton, Alberta, 231 pp.

Irwin, H., Curtis, C., Coleman, M., 1977. Isotopic evidence for source of diagenetic carbonates formed during burial carbonates formed during burial of organic-rich sediments. Nature 269, 209-213.

Jacka, A.D., 1974. Replacement of fossils by length-slow chalcedony and associated dolomitization. Journal of Sedimentary Petrology 44, 421-427.

James, N.P., Bone, Y., 1992. Synsedimentary cemented calcarenite layers in Oligo-Miocene cool water shelf limestones, Eucla Platform, Southern Australia. Journal of Sedimentary Petrology 62, 860-872.

James, N.P., Bone, Y., Kyser, T.K., 1993. Shallow burial dolomitization and dedolomitization of mid-Cenozoic, cool-water, calcitic, deep-shelf limestones, Southern Australia. Journal of Sedimentary Petrology 63, 528-538.

Jiang, H., Lai, X., Luo, G., Aldridge, R., Zhang, K., Wignall, P., 2007. Restudy of conodont zonation and evolution across the P/T boundary at Meishan section, Changxing, Zhejiang, China. Global and Planetary Change 55, 39-55.

Jiang, H., Lai, X., Yan, C., Aldridge, R.J., Wignall, P., Sun, Y., 2011. Revised conodont zonation and conodont evolution across the Permian-Triassic boundary at the Shangsi section, Guangyuan, Sichuan, South China. Global and Planetary Change 77, 103-115.

Jiang, L., Worden, R.H., Cai, C., Li, K., Xiang, L., Cai, L., He, X., 2014. Dolomitization of gas reservoirs: The Upper Permian Changxing and Lower Triassic Feixianguan Formations, Northeast Sichuan Basin, China. Journal of Sedimentary Research 84, 792-815.

Jin, Y.G., Wang, Y., Wang, W., Shang, Q.H., Cao, C.Q., Erwin, D.H., 2000. Pattern of marine mass extinction near the Permian-Triassic boundary in South China. Science 289, 432-436.

Jones, B., 2005. Dolomite crystal architecture: Genetic implications for the origin of the tertiary dolostones of the Cayman Islands. Journal of Sedimentary Research 75, 177-189.

Jones, B., 2007. Inside-out dolomite. Journal of Sedimentary Research 77, 539-551.

Jones, B., Luth, R.W., 2002. Dolostones from Grand Cayman, British West Indies. Journal of Sedimentary Research 72, 559-569.

Jones, B., Pleydell, S.M., Ng, K.C., Longstaffe, F.J., 1989. Formation of Poikilotopic Calcite-Dolomite Fabrics in the Oligocene-Miocene Bluff Formation of Grand-Cayman, British-West-Indies. Bulletin of Canadian Petroleum Geology 37, 255-265.

Kah, L.C., 2000. Depositional $\delta^{18}O$ signatures in Proterozoic dolostones: Constraints on seawater chemistry and early diagenesis. In: J.P. Grotzinger, N.P. James (Eds.), Carbonate Sedimentation and Diagenesis in the Evolving Precambrian World. SEPM Special Publication 67, pp. 345-360.

Kearsey, T., Twitchett, R.J., Price, G.D., Grimes, S.T., 2009. Isotope excursions and palaeotemperature estimates from the Permian/Triassic boundary in the Southern Alps (Italy). Palaeogeography Palaeoclimatology Palaeoecology 279, 29-40.

Korte, C., Kozur, H.W., 2010. Carbon-isotope stratigraphy across the Permian-Triassic boundary: a review. Journal of Asian Earth Sciences 39, 215-235.

Korte, C., Jasper, T., Kozur, H.W., Veizer, J., 2005a. $\delta^{18}O$ and $\delta^{13}C$ of Permian brachiopods: A record of seawater evolution and continental glaciation. Palaeogeography Palaeoclimatology Palaeoecology 224, 333-351.

Korte, C., Kozur, H.W., Joachimski, M.M., Strauss, H., Veizer, J., Schwark, L., 2004. Carbon, sulfur, oxygen and strontium isotope records, organic geochemistry and biostratigraphy across the Permian/Triassic boundary in Abadeh, Iran. International Journal of Earth Sciences 93, 565-581.

Korte, C., Kozur, H.W., Veizer, J., 2005b. $\delta^{13}C$ and $\delta^{18}O$ values of Triassic brachiopods and carbonate rocks as proxies for coeval seawater and palaeotemperature. Palaeogeography Palaeoclimatology Palaeoecology 226, 287-306.

Kyser, K., James, N.P., Bone, Y., 2002. Shallow burial dolomitization and dedolomitization of Cenozoic cool-water limestones, southern Australia: Geochemistry and origin. Journal of Sedimentary Research 72, 146-157.

Land, L.S., 1980. The isotopic and trace element geochemistry of dolomite: the state of the art. In: D.H. Zenger, J.B. Dunham, R.L. Ethington (Eds.), Concepts and Models of Dolomitization. SEPM Special Publication 28, pp. 87-110.

Land, L.S., Prezbindowski, D.R., 1981. The origin and evolution of saline formation water, Lower Cretaceous carbonates, south-central Texas, U.S.A. Journal of Hydrology 54, 51-74.

Lee, M.R., Harwood, G.M., 1989. Dolomite calcitization and cement zonation related to uplift of the Raisby Formation (Zechstein carbonate), northeast England. Sedimentary Geology 65, 285-305.

Lee, X., Wan, G., 2000. No vital effect on $\delta^{18}O$ and $\delta^{13}C$ values of fossil brachiopod shells, Middle Devonian of China. Geochimica et Cosmochimica Acta 64, 2649-2664.

Li, R., Jones, B., 2013. Heterogeneous diagenetic patterns in the Pleistocene Ironshore Formation of Grand Cayman, British West Indies. Sedimentary Geology 294, 251-265.

Longman, M.W., Mench, P.A., 1978. Diagenesis of Cretaceous limestones in the Edwards aquifer system of south-central Texas: A scanning electron microscope study. Sedimentary Geology 21, 241-276.

Lowenstam, H.A., 1961. Mineralogy, O^{18}/O^{16} ratios, and strontium and magnesium contents of recent and fossil brachiopods and their bearing on the history of the oceans. The Journal of Geology 69, 241-260.

Luo, G., Wang, Y., Algeo, T.J., Kump, L.R., Bai, X., Yang, H., Yao, L., Xie, S., 2011. Enhanced nitrogen fixation in the immediate aftermath of the latest Permian marine mass extinction. Geology 39, 647-650.

Macouin, M., Ader, M., Moreau, M., Poitou, C., Yang, Z., Sun, Z., 2012. Deciphering the impact of diagenesis overprint on negative 13C excursions using rock magnetism: Case study of Edicaran carbonates, Yangjiaping section, South China. Earth and Planetary Science Letters 351-352, 281-294.

Magaritz, M., Kafri, U., 1981. Stable isotope and Sr2+/Ca2+ evidence of diagenetic dedolomitization in a schizohaline environment: Cenomanian of northern Israel. Sedimentary Geology 28, 29-41.

Major, R.P., Lloyd, R.M., Lucia, F.J., 1992. Oxygen isotope composition of Holocene dolomite formed in a humid hypersaliine setting. Geology 20, 586-588.

McHargue, T.R., Price, R.C., 1982. Dolomite from clay in argillaceous or shale-associated marine carbonates. Journal of Sedimentary Petrology 52, 873-886.

McLennan, S.M., 1989. Rare earth elements in sedimentary rocks: Influence of provenance and sedimentary processes. In: B.R. Lipin, G.A. McKay (Eds.), Geochemistry and Mineralogy of Rare Earth Elements: Reviews in Mineralogy 21. Mineralogical Society of America, pp. 169-200.

Melim, L.A., Swart, P.K., Eberli, G.P., 2004. Mixing-zone diagenesis in the subsurface of Florida and the Bahamas. Journal of Sedimentary Research 74, 904-913.

Mii, H., Grossman, E.L., Yancey, T.E., 1997. Stable carbon and oxygen isotope shifts in Permian seas of West Spitsbergen-Global change or diagenetic artifact? Geology 25, 227-230.

Mu, X., Riding, R., 1988. Silicification of Permian calcareous algae from Nanjing, China. Geological Magazine 125, 123-139.

Muchez, P., Hein, U.F., Van Den Broeck, K., Vandecasteele, C., 1994. Lithological influence on the composition of vein cements in the Carboniferous of the Campine Basin (northern Belgium). European Journal of Mineralogy 6, 985-994.

Muller, G., 1967. Chapter 4 Diagenesis in Argillaceous Sediments. In: G. Larsen, G.V. Chilingar (Eds.), Diagenesis in Sediments. Developments in Sedimentology 8, pp. 127-177.

Newell, N.D., 1967. Revolutions in the history of life. Geological Society of America Special Papers 89, 63-92.

Nicolaides, S., Wallace, M.W., 1997. Submarine cementation and subaerial exposure in Oligo-Miocene temperate carbonates, Torquay Basin, Australia. Journal of Sedimentary Research 67, 397-410.

Nothdurft, L.D., Webb, G.E., Kamber, B.S., 2004. Rare earth element geochemistry of Late Devonian reefal carbonates, Canning basin, Western Australia: Confirmation of a seawater REE proxy in ancient limestones. Geochimica et Cosmochimica Acta 68, 263-283.

Oehlert, A.M., Swart, P.K., 2014. Interpreting carbonate and organic carbon isotope covariance in the sedimentary record. Nature Communications 5, 1-7.

Popp, B.N., Anderson, T.F., Sandberg, P.A., 1986. Brachiopods as indicators of original isotopic compositions in some Paleozoic limestones. Geological Society of America Bulletin 97, 1262-1269.

Purser, B.H., Brown, A., Aissaoui, D.M., 1994. Nature, origins and evolution of porosity in dolomites. In: B.H. Purser, M.E. Tucker, D.H. Zenger (Eds.), Dolomites: A Volume in Honour of Dolomieu. The International Association of Sedimentologists Special Publications 21. The International Association of Sedimentologists, pp. 283-308.

Reinhold, C., 1998. Multiple episodes of dolomitization and dolomite recrystallization during shallow burial in Upper Jurassic shelf carbonates: eastern Swabian Alb, southern Germany. Sedimentary Geology 121, 71-95.

Schauer, M., Aigner, T., 1997. Cycle stacking pattern, diagenesis and reservoir geology of peritidal dolostones, Trigonodus-Dolomite, Upper Muschelkalk (Middle Trassic, SW-Germany). Facies 37, 23-25.

Schobben, M., Ullmann, C.V., Leda, L., Korn, D., Struck, U., Reimold, W.U., Ghaderi, A., Algeo, T.J., Korte, C., 2016. Discerning primary versus diagenetic signals in carbonate carbon and oxygen isotope records: An example from the Permian-Triassic boundary of Iran. Chemical Geology 422, 94-107.

Scholle, P.A., 1971. Diagenesis of deep-water carbonate turbidites, Upper Cretaceous Monte Antola Flysch, Northern Apennines, Italy. Journal of Sedimentary Petrology 41, 233-250.

Scholle, P.A., Ulmer-Scholle, D.S., 2003. A Color Guide to the Petrography of

Carbonate Rocks: Grains, Textures, Porosity, Diagenesis. AAPG Memoir 77. The American Association of Petroleum Geologists, Tulsa, Oklahoma, USA, 459 pp.

Shen, S., Crowley, J.L., Wang, Y., Bowring, S.A., Erwin, D.H., Sadler, P.M., Cao, C., Rothman, D.H., Henderson, C.M., Ramezani, J., Zhang, H., Shen, Y., Wang, X., Wang, W., Mu, L., Li, W., Tang, Y., Liu, X., Liu, L., Zeng, Y., Jiang, Y., Jin, Y., 2011. Calibrating the end-Permian mass extinction. Science 334, 1367-1372.

Shields, G.A., Webb, G.E., 2004. Has the REE composition of seawater changed over geological time? Chemical Geology 204, 103-107.

Sholkovitz, E.R., Landing, W.M., Lewis, B.L., 1994. Ocean particle chemistry: the fractionation of rare earth elements between suspended particles and seawater. Geochimica et Cosmochimica Acta 58, 1567-1579.

Sibley, D.F., Gregg, J.M., 1987. Classification of dolomite rock textures. Journal of Sedimentary Petrology 57, 967-975.

Song, H., Tong, J., Xiong, Y., Sun, D., Tian, L., Song, H., 2012. The large increase of $\delta^{13}C_{carb}$-depth gradient and the end-Permian mass extinction. Science China-Earth Sciences 55, 1101-1109.

Song, H., Tong, J., Algeo, T.J., Horacek, M., Qiu, H., Song, H., Tian, L., Chen, Z., 2013. Large vertical $\delta^{13}C_{DIC}$ gradients in Early Triassic seas of the South China craton: Implications for oceanographic changes related to Siberian Traps volcanism. Global and Planetary Change 105, 7-20.

Song, H., Tong, J., Algeo, T.J., Song, H., Qiu, H., Zhu, Y., Tian, L., Bate, S., Lyons, T.W., Luo, G., Kump, L.R., 2014. Early Triassic seawater sulfate drawdown. Geochimica et Cosmochimica Acta 128, 95-113.

Song, H., Wignall, P.B., Tong, J., Song, H., Chen, J., Chu, D., Tian, L., Luo, M., Zong, K., Chen, Y., Lai, X., Zhang, K., Wang, H., 2015. Integrated Sr isotope variations and global environmental changes through the Late Permian to early Late Triassic. Earth and Planetary Science Letters 424, 140-147.

Spötl, C., Burns, S.J., 1991. Formation of ^{18}O-depleted dolomite within a marine evaporitic sequence, Triassic Reichenhall Formation, Austria. Sedimentology 38, 1041-1057.

Swart, P.K., 2008. Global synchronous changes in the carbon isotopic composition of carbonate sediments unrelated to changes in the global carbon cycle. Proceedings of the National Academy of Sciences of the United States of America 105, 13741-

13745.

Swart, P.K., Kennedy, M.J., 2012. Does the global stratigraphic reproducibility of ^{13}C in Neoproterozoic carbonates require a marine origin? A Pliocene-Pleistocene comparison. Geology 40, 87-90.

Swart, P.K., Cantrell, D.L., Westphal, H., Handford, C.R., Kendall, C.G., 2005. Origin of dolomite in the Arab-D reservoir from the Ghawar field, Saudi Arabia: Evidence from petrographic and geochemical constraints. Journal of Sedimentary Research 75, 476-491.

Taylor, T.R., Sibley, D.F., 1986. Petrographic and geochemical characteristics of dolomite types and the origin of ferroan dolomite in the Trenton Formation, Ordovician, Michigan Basin, U.S.A. Sedimentology 33, 61-86.

Tong, J., Yin, H., Yang, Y., 1996. Permian and Triassic boundary serial section of Meishan, Changxing, Zhejiang Province. Geoscience 10, 325-329. (in Chinese)

Torok, A., 2000. Formation of dolomite mottling in Middle Triassic ramp carbonates (Southern Hungary). Sedimentary Geology 131, 131-145.

Vasconcelos, C., McKenzie, J.A., 1997. Microbial mediation of modern dolomite precipitation and diagenesis under anoxic conditions (Lagoa Vermelha, Rio De Janeiro, Brazil). Journal of Sedimentary Research 67, 378-390.

Vasconcelos, C., McKenzie, J.A., Bernasconi, S.M., Grujic, D., Tiens, A.J., 1995. Microbial mediation as a possible mechanism for natural dolomite formation at low temperatures. Nature 377, 220-222.

Vasconcelos, C., McKenzie, J.A., Warthmann, R., Bernasconi, S.M., 2005. Calibration of the $\delta^{18}O$ paleothermometer for dolomite precipitated in microbial cultures and natural environments. Geology 33, 317-320.

Veizer, J., Hoefs, J., 1976. The nature of O_{18}/O^{16} and C^{13}/C^{12} secular trends in sedimentary carbonate rocks. Geochimica et Cosmochimica Acta 40, 1387-1395.

Wignall, P.B., Kershaw, S., Collin, P., Crasquin-Soleau, S., 2009. Erosional truncation of uppermost Permian shallow-marine carbonates and implications for Permian-Triassic boundary events: Comment. GSA Bulletin 121, 954-956.

Worden, R.H., Morad, S., 2003. Clay minerals in sandstones: controls on formation, distribution and evolution. In: R.H. Worden, S. Morad (Eds.), Clay Mineral Cements in Sandstones. International Association of Sedimentologists Special Publication 34. International Association of Sedimentologists, pp. 3-41.

Wray, D.S., 1995. Origin of clay-rich beds in Turonian chalks from Lower Saxony, Germany - A rare-earth element study. Chemical Geology 119, 161-173.

Wu, Y., Jiang, H., Liao, T., 2006. Sea-level drops in the Permian-Triassic boundary section at Laolongdong, Chongqing, Sichuan province. Acta Petrologica Sinica 22, 2405-2412.

Wu, Y., Yuan, X., Jiang, H., Liu, L., 2014. Coevality of the sea-level fall and main mass extinction in the Permian-Triassic transition in Xiushui, Jiangxi Province, southern China. Journal of Palaeogeography 3, 309-322.

Yin, H., Wu, S., Din, M., Zhang, K., Tong, J., Yang, F., 1994. The Meishan section, candidate of the global stratotype section and point (GSSP) of the Permian-Triassic boundary (PTB). Albertiana 14, 15-31.

Yin, H., Jiang, H., Xia, W., Feng, Q., Zhang, N., Shen, J., 2014. The end-Permian regression in South China and its implication on mass extinction. Earth-Science Reviews 137, 19-33.

Yin, H., Zhang, K., Tong, J., Yang, Z., Wu, S., 2001. The global stratotype section and point (GSSP) of the Permian-Triassic boundary. Episodes 24, 102-114.

Yin, H., Xie, S., Luo, G., Algeo, T.J., Zhang, K., 2012. Two episodes of environmental change at the Permian-Triassic boundary of the GSSP section Meishan section. Earth-Science Reviews 115, 163-172.

Yoo, C.M., Lee, Y.I., 1998. Origin and modification of early dolomites in cyclic shallow platform carbonates, Yeongheung Formation (middle Ordovician), Korea. Sedimentary Geology 118, 141-157.

Zentmyer, R.A., Pufahl, P.K., James, N.P., Hiatt, E.E., 2011. Dolomitization on an evaporitic Paleoproterozoic ramp: Widespread synsedimentary dolomite in the Denault Formation, Labrador Trough, Canada. Sedimentary Geology 238, 116-131.

Zhang, K., Tong, J., Hou, G., Wu, S., Zhu, Y., Lin, Q., 2005. Regional Geological Report, the People's Republic of China (Meishanzhen Map H50E006023, Changxingian Map, H50E006024, Scale: 1:50000). China University of Geosciences Press, Wuhan, 264 pp. (in Chinese)

Zhang, K., Tong, J., Yin, H., Wu, S., 1997. Sequence stratigraphy of the Permian-Triassic boundary section of Changxing, Zhejiang, Southern China. Acta Geologica Sinica 71, 90-103.

Zheng, Q., Cao, C., Zhang, M., 2013. Sedimentary features of the Permian-Triassic boundary sequence of the Meishan section in Changxing County, Zhejiang Province. Science China-Earth Sciences 56, 956-969.

FIGURE CAPTIONS

Figure 1. Correlation of $\delta^{13}C$ data for PTB intervals from five sections. The biostratigraphic frame for Meishan is based on Jiang et al. (2007) and Yin et al. (2014). The age for claystone beds 25 and 28 came from Shen et al. (2011). Red line = Permian-Triassic boundary (PTB), green line = extinction event horizon. The carbon isotope data for Meishan section came from Jin et al. (2000), Shangsi section from Korte and Kozur (2010), Abadeh section from Korte et al. (2004), Pufels section from Horacek et al. (2007), Tesero section, Italy from Broglio Loriga and Cassinis (1992).

Figure 2. Location of Meishan section. (**A**) Exposure of sections A, B, C, D, E, and Z in the Meishan quarry. Map showing location of **(B)** Changxing County in Zhejiang Province and **(C)** Meishan village northwest of Changxing.

Figure 3. The lithology and bulk sample stable isotopic profiles of the GSSP Meishan section (modified from Tong et al., 2005; Zhang et al., 2005). Inset indicates position of profile in Figure 4.

Figure 4. The lithology, mineralogy, stable isotopic composition, and elemental profiles of Beds 24 to 62 covering the topmost unit of Changhsing Formation and the Yinkeng Formation (Beds 25 to 60).

Figure 5. Slab of Bed 27 from Section A, showing the six lithological layers (I to VI). White arrows indicate the firmground lithoclasts.

Figure 6. Backscatter electron images of dolomite crystals. **(A)** Layer VI of Bed 27. Irregular contact between zoned dolomite crystals. **(B)** Zoned dolomite crystal with LCD core encased successively by zones of calcite (cc) and HCD. Note the irregular outline of calcite zone. **(C)** Layer V of Bed 27. Subhedral to euhedral dolomite crystals in the matrix. **(D, E)** Zoned dolomite crystal with LCD core encased successively by zones of calcite, HCD, and ferroan HCD (Fe-HCD). Note the irregular outline of calcite zone. **(F)** The zoned dolomite crystal showing irregular calcite zone.

Figure 7. BSE images of dolomite crystals from Meishan section. White lines indicate EMP analysis transects shown in panel D. (**A**) Zoned dolomite crystals showing ferroan LCD core encased by HCD cortice. (**B**) Zoned dolomite crystals showing LCD core encased by HCD cortice. (**C**) Zoned dolomite crystals showing LCD core encased by calcite cortice. (**D**) %Ca, as determined by EMPA, along transects AA', BB', and CC' in dolomite crystals shown in panels A, B, and C. (**E**) Frequency histogram showing two groups of mol% $CaCO_3$ in dolomite (EMPA analysis) from Meishan section.

Figure 8. SEM (A-B) and BSE (C-F) images of dolomite crystals in Bed 27. cc = calcite, chl = chlorite. **(A)** Hollow dolomite crystal with prismatic calcite growing in the void. **(B)** Hollow dolomite crystal with void filled with rhombic calcite crystals. **(C)** Hollow dolomite crystal. **(D, E)** Rhombic calcite crystals. **(F)** Rhombic crystal with LCD core encased by calcite cortex.

Figure 9. Diagenetic fabrics in Bed 24. **(A)** Calcite cement (indicated by black arrows) between skeletal grains. **(B-D)** Silica cement, silicification of skeletal grains,

and the chambers of allochems being filled with calcite. **(E)** Recrystallization of skeletal grains displaying concave-convex contact between grains. **(F)** Moldic porosity (indicated by black arrows).

Figure 10. Cathodoluminescence (CL) images of samples from Beds 24 to 62, Meishan Section. (**A**) Image under plane polarized light (PPL). Very fine dolomite crystals floating in argillaceous groundmass. (**B**) Same panel to A under CL, showing dolomite crystals with non-luminescent core and dull-orange luminescent cortice. Note that the brachiopod shell in the upper right corner displays non-luminescence. (**C**) Image under PPL. Fragment of brachiopod shell floating in argillaceous groundmass. (**D**) Same panel to C under CL, showing brachiopod shells with dull-orange to orange luminescence. (**E**) CL image showing non-luminescence for groundmass in Bed 24. Some crinoid fragment and calcite cement display orange luminescence. (**F**) Dull-orange luminescence for groundmass in Bed 24. The luminescence of allochem grains ranges from non-luminscence to dull to bright orange.

Figure 11. Variation in the $\delta^{13}C$ values with $\delta^{18}O$ values for the samples in Beds 24 to 62, Meishan section. Note the dash line decribing the positive correlation between $\delta^{13}C$ and $\delta^{18}O$ of samples from dolomite-bearing beds.

Figure 12. Cross plots of geochemical attributes ($\delta^{13}C$, $\delta^{18}O$, Mn, Sr, Mn/Sr, dolomite content, and clay mineral content) for bulk carbonate samples from Beds 24 to 62.

Figure 13. Shale-normalized REY patterns of (**A**) dolomite, brachiopod shells, and (**B**) bulk rock samples in carbonate succession from Meishan section.

Figure 14. Schematic diagram summarizing the diagenetic evolution of dolomite crystals in Beds 27 to 62, Meishan section.

Figure 15. Cross plots of $\delta^{13}C$ and $\delta^{18}O$ compositions of PTB intervals from collected global sections, which were formed in depositional setting ranging from shallow water depth to deeper water depth.

Figure
Click here to download high resolution image

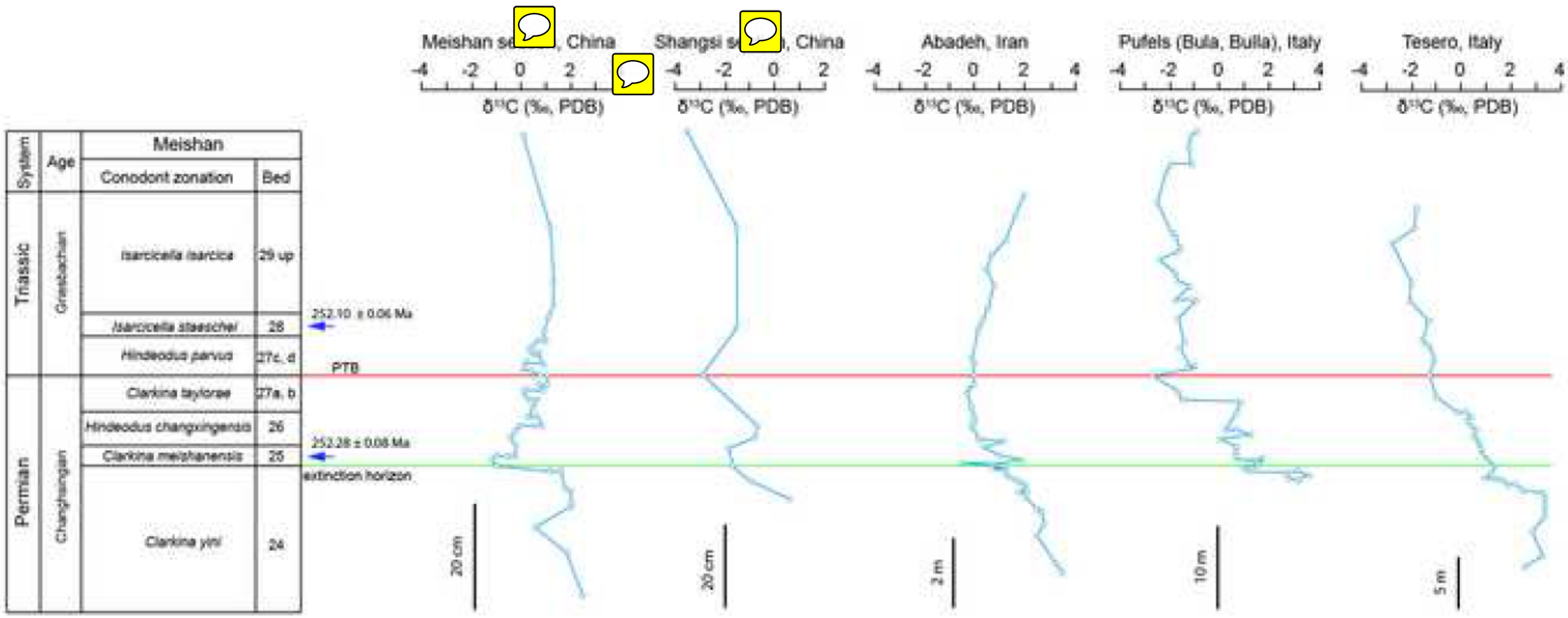

Figure

Click here to download high resolution image

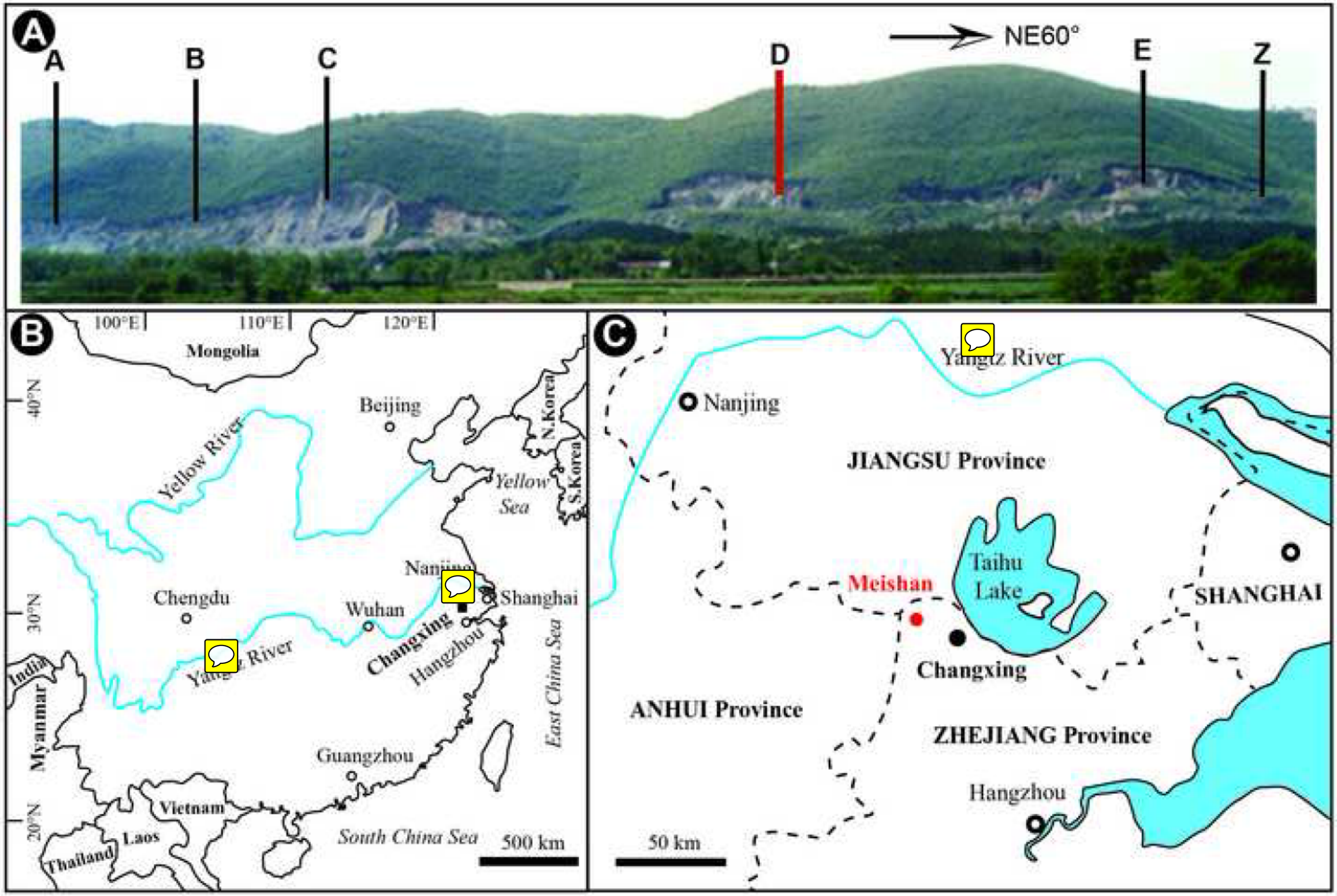

Figure

Click here to download high resolution image

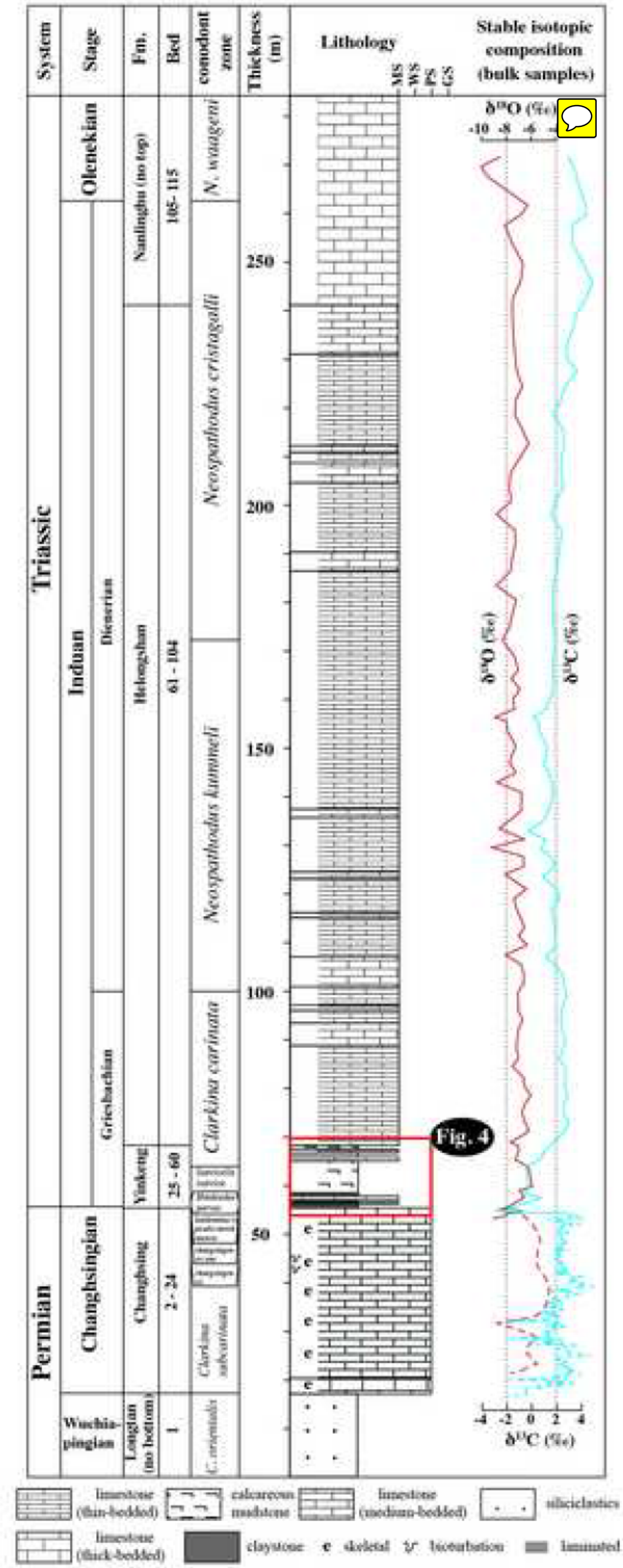

Figure
Click here to download high resolution image

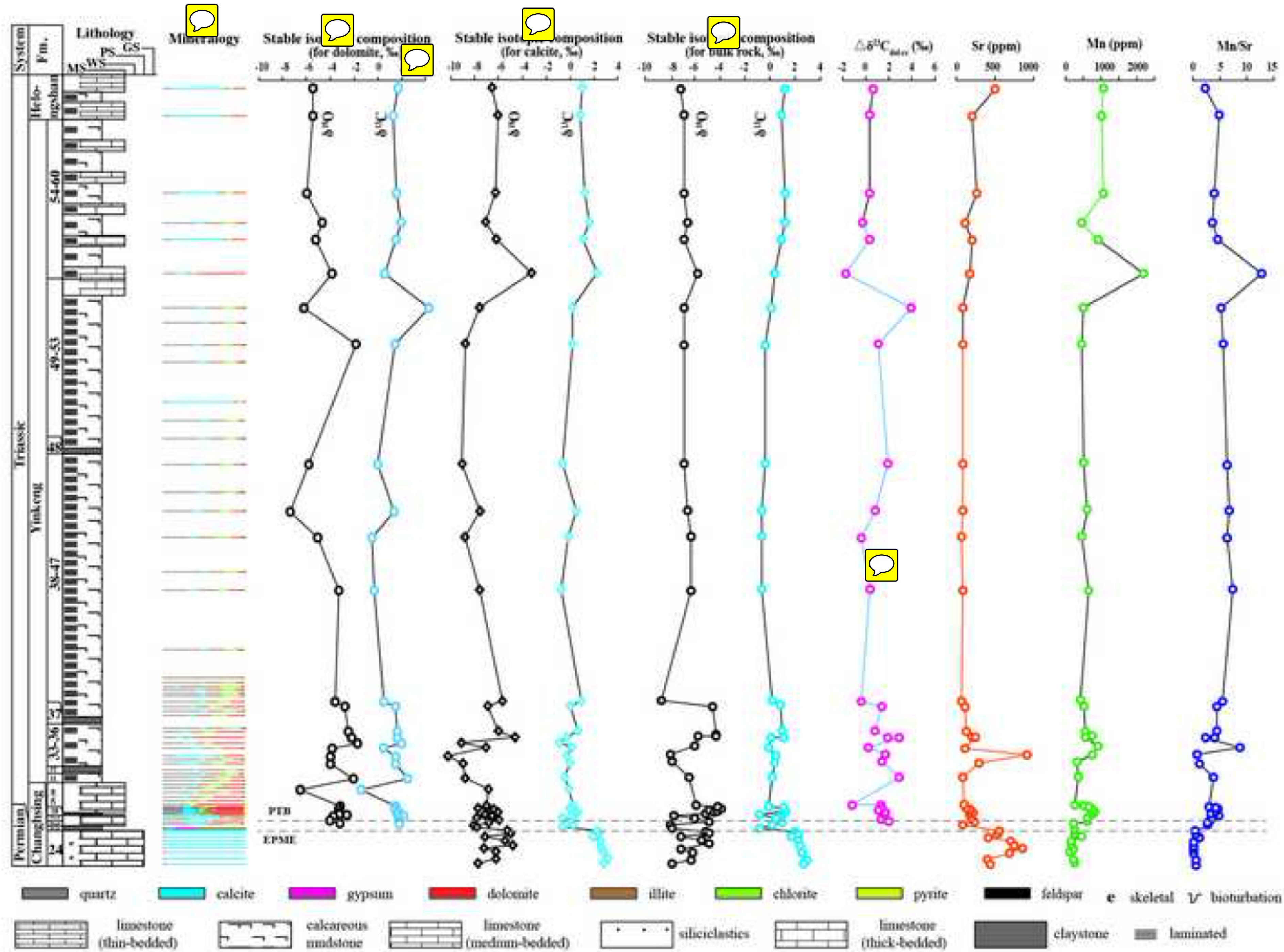

Figure
Click here to download high resolution image

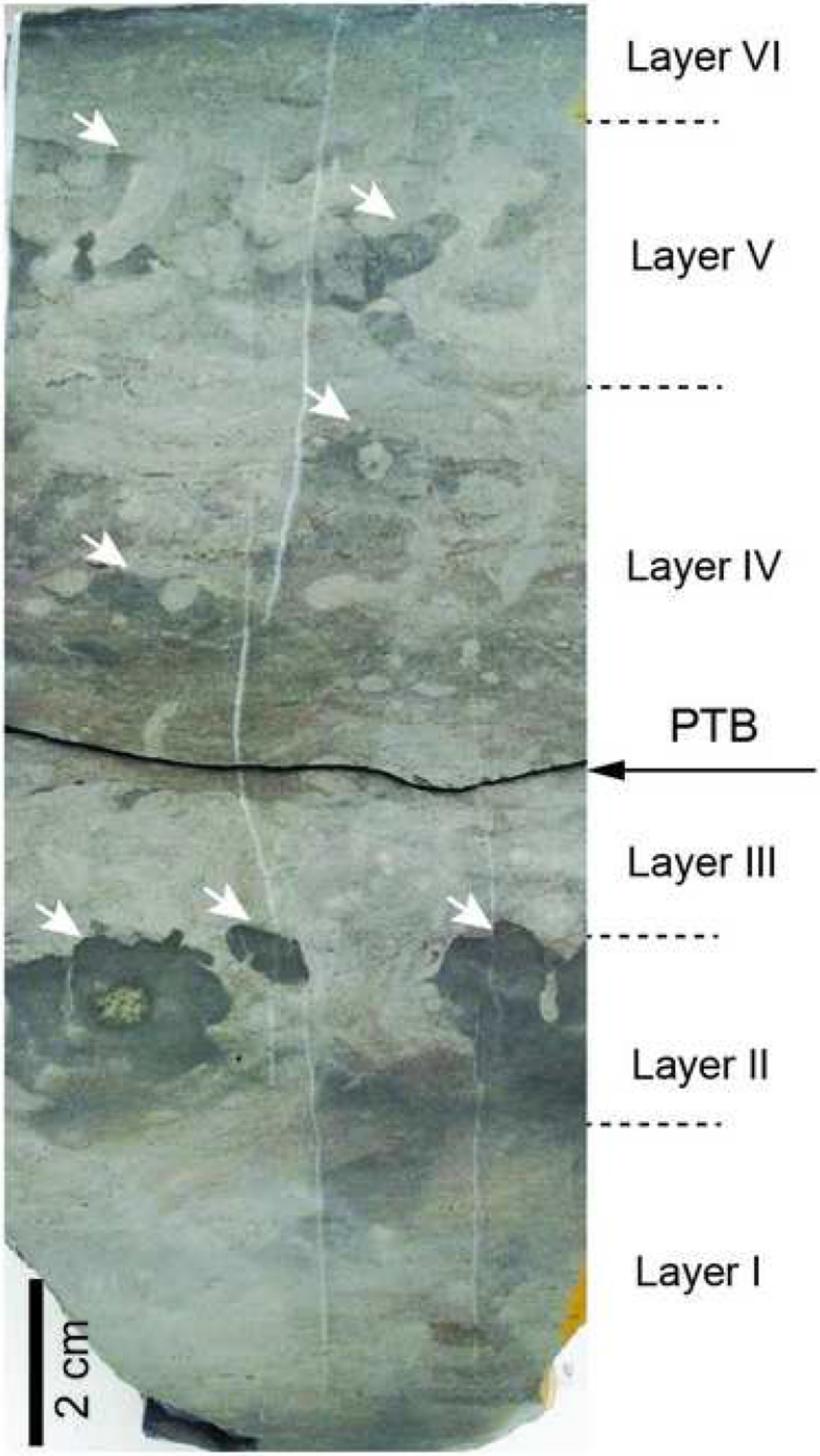

Figure
Click here to download high resolution image

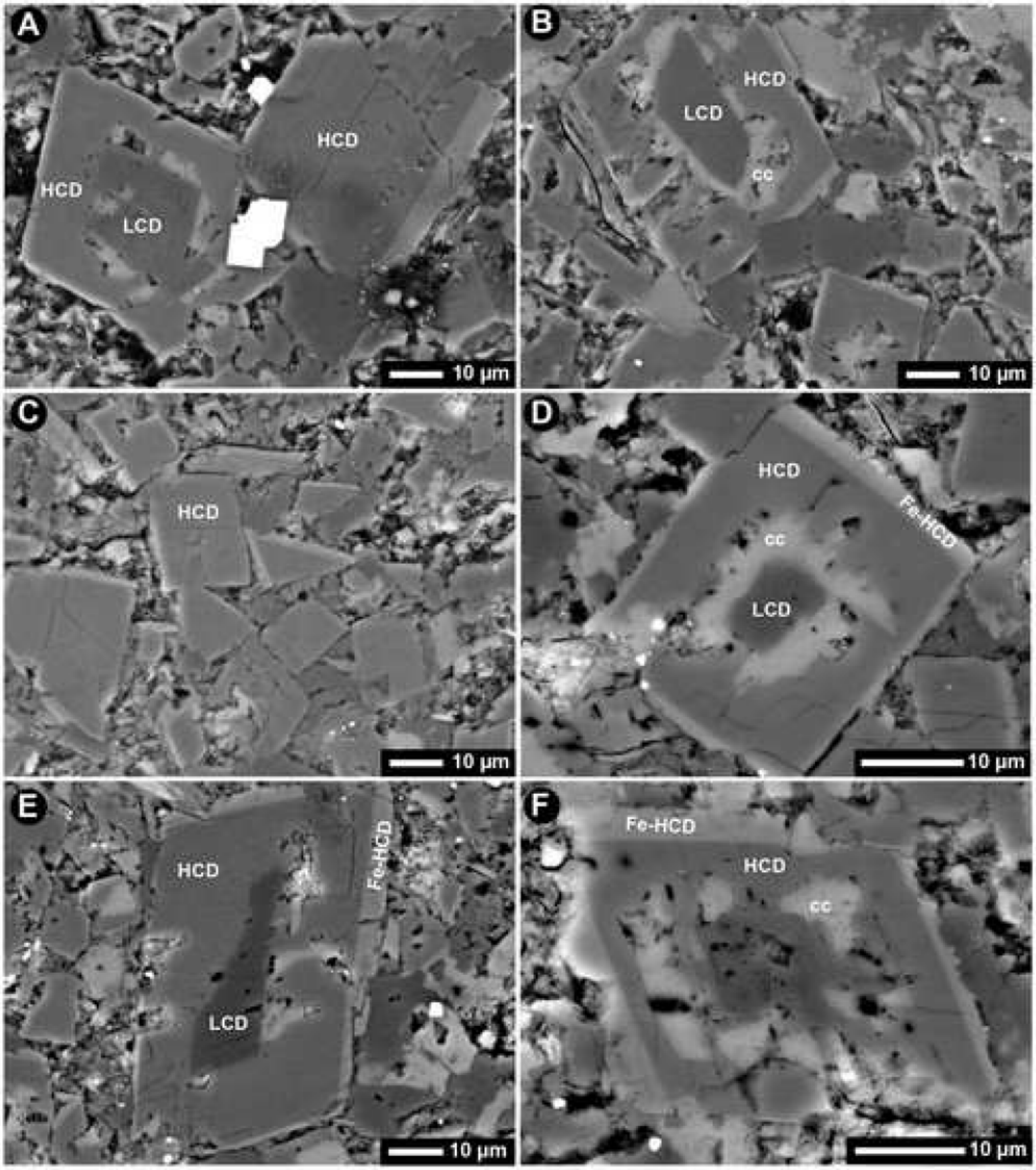

Figure

Click here to download high resolution image

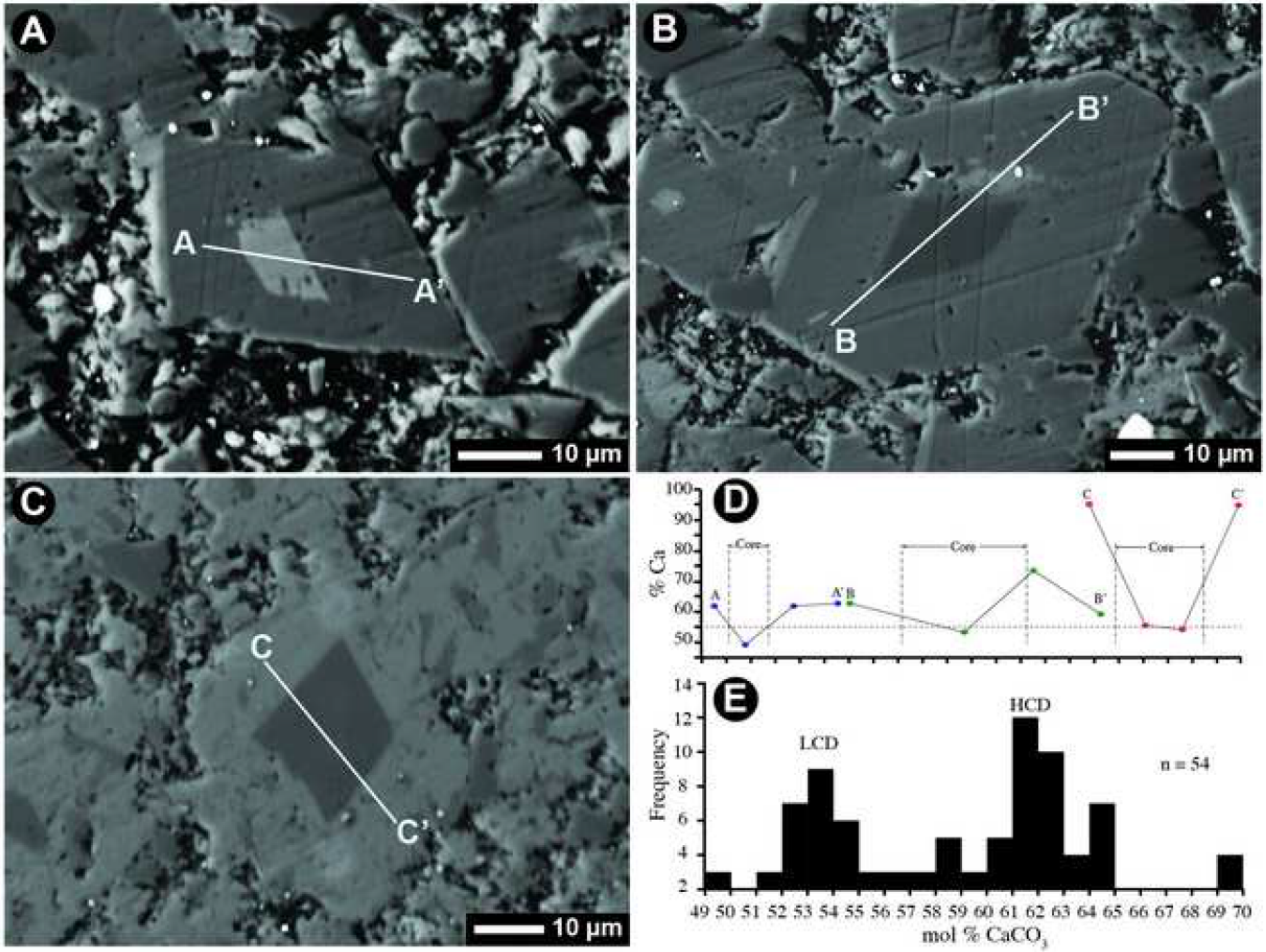

Figure

Click here to download high resolution image

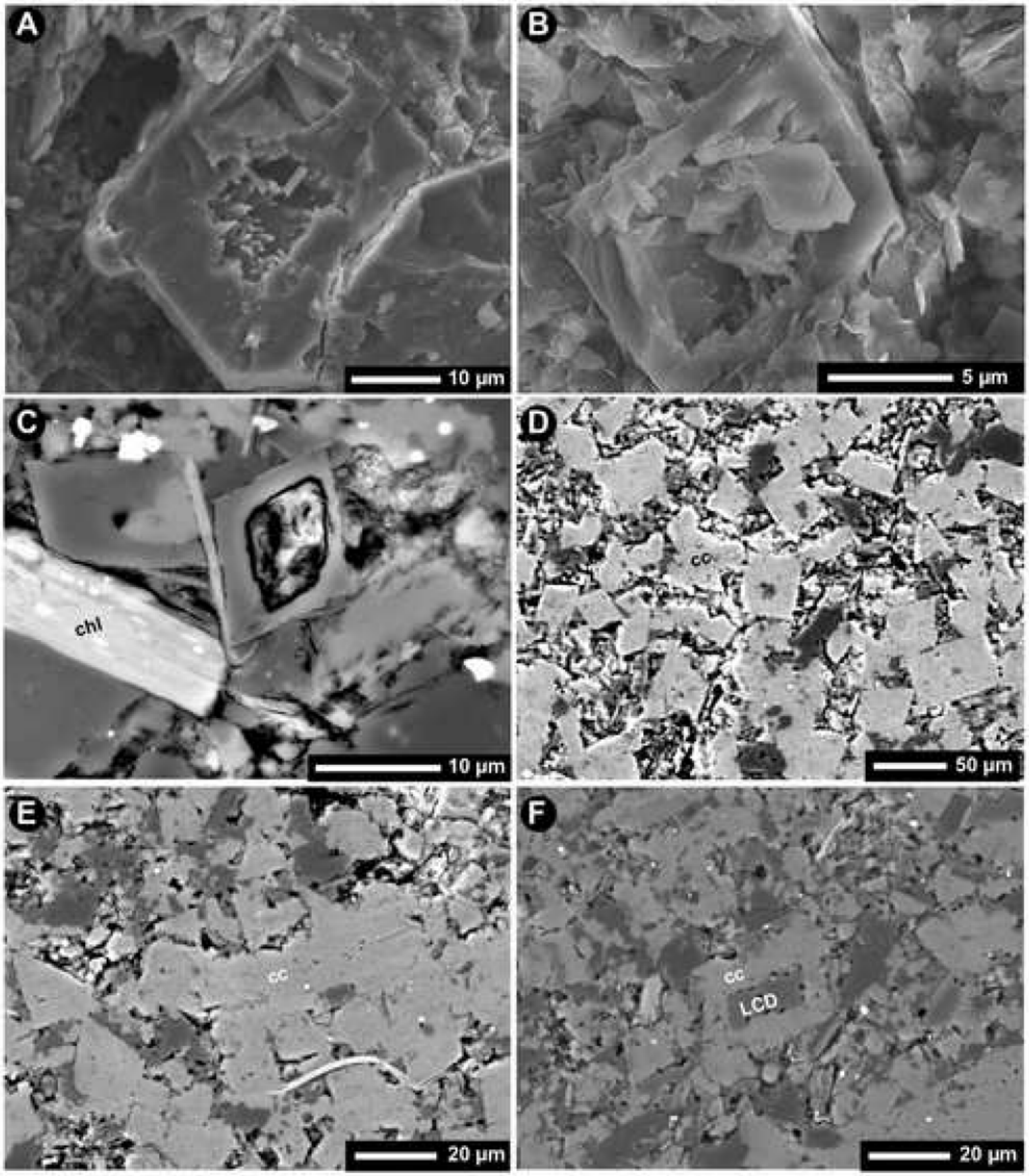

Figure

Click here to download high resolution image

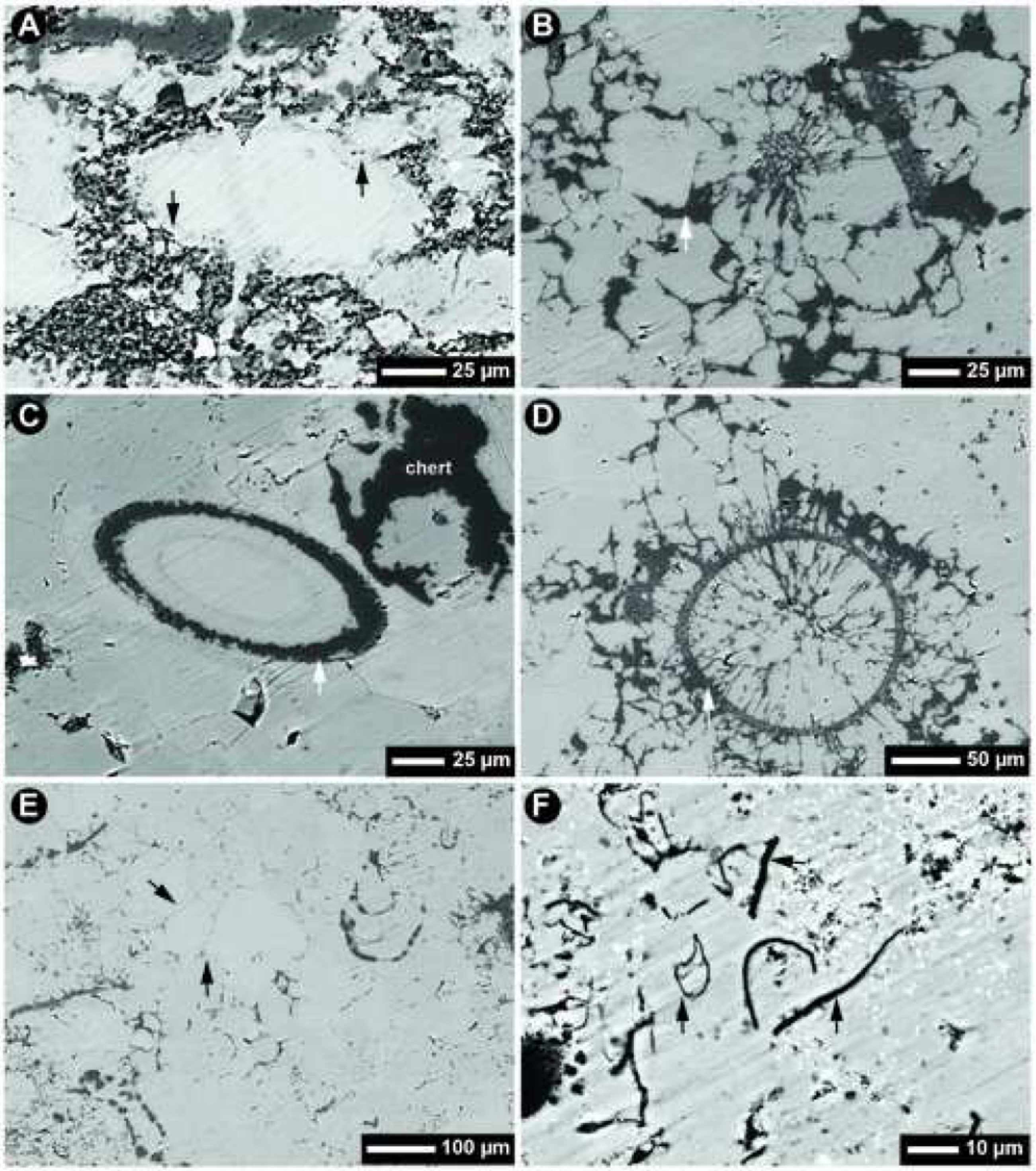

Figure
Click here to download high resolution image

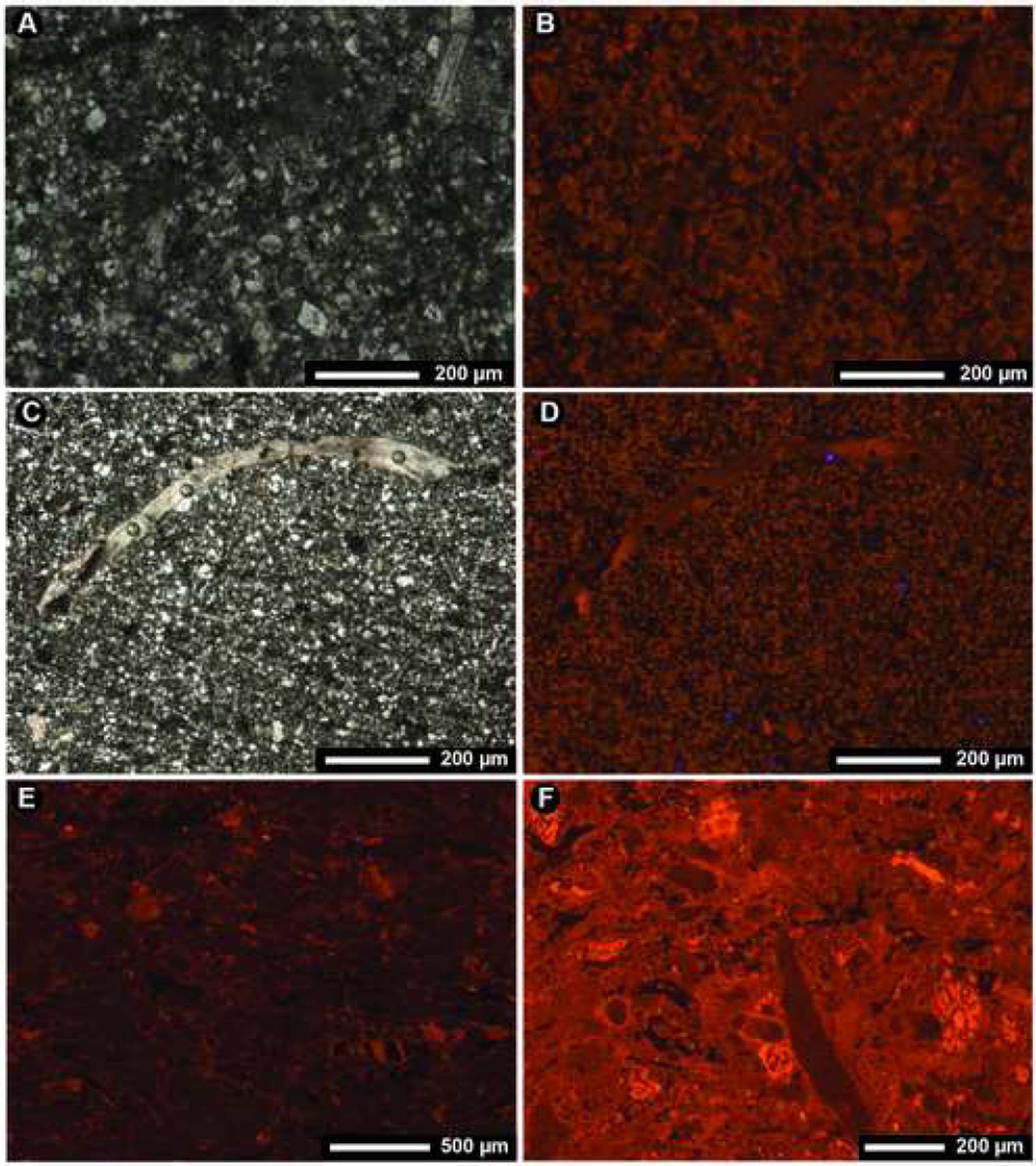

Figure

Click here to download high resolution image

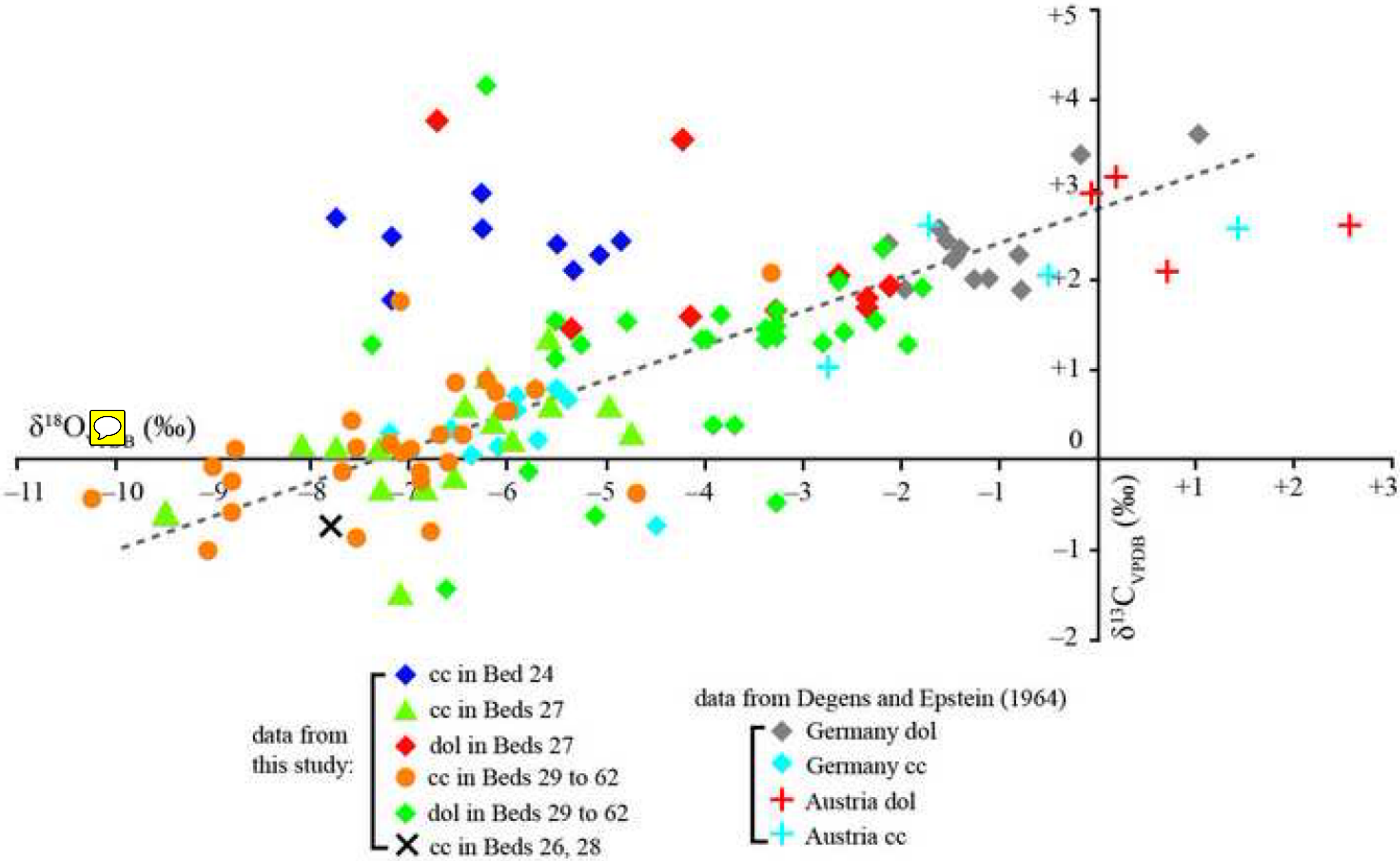

Figure
Click here to download high resolution image

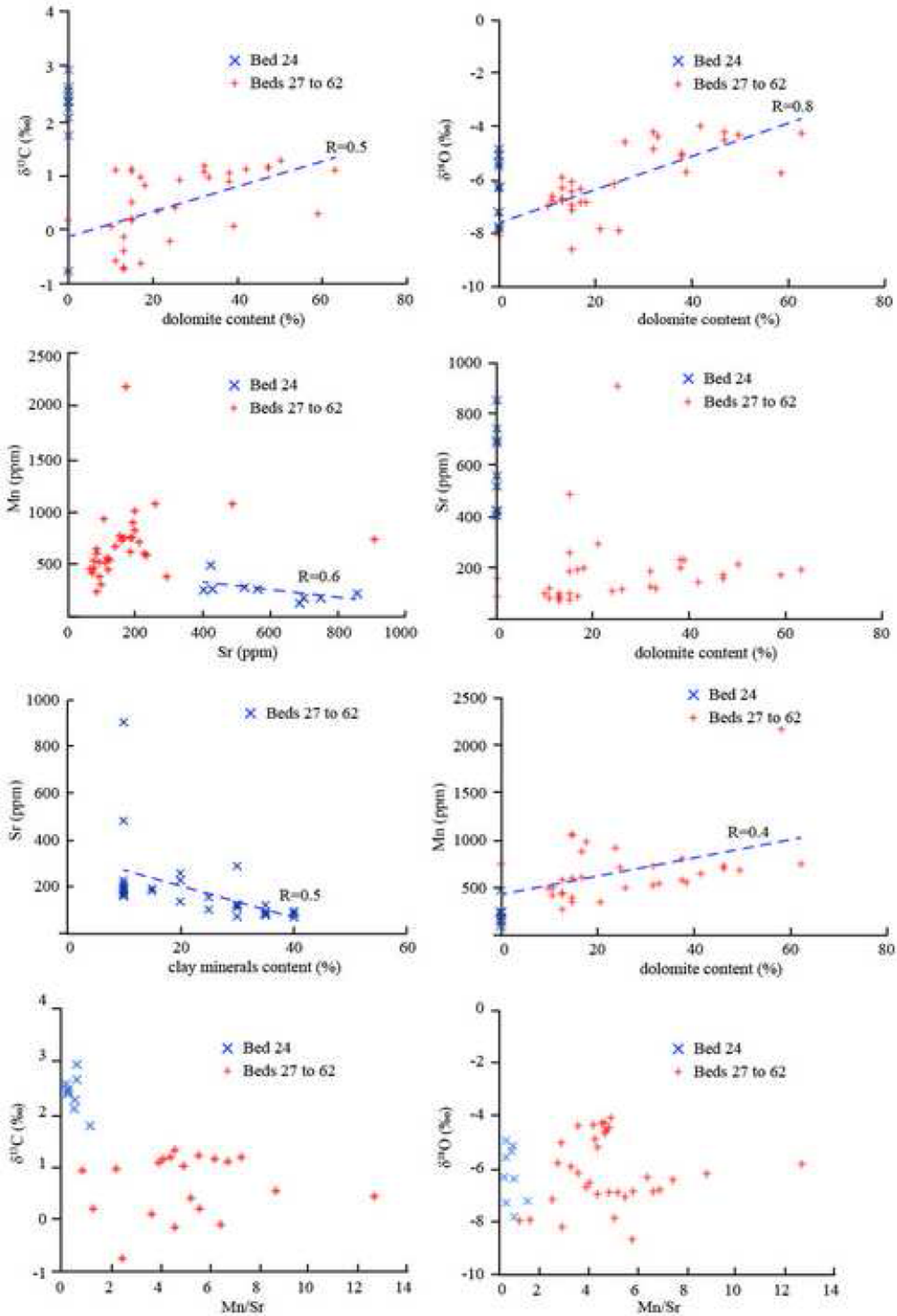

Figure
Click here to download high resolution image

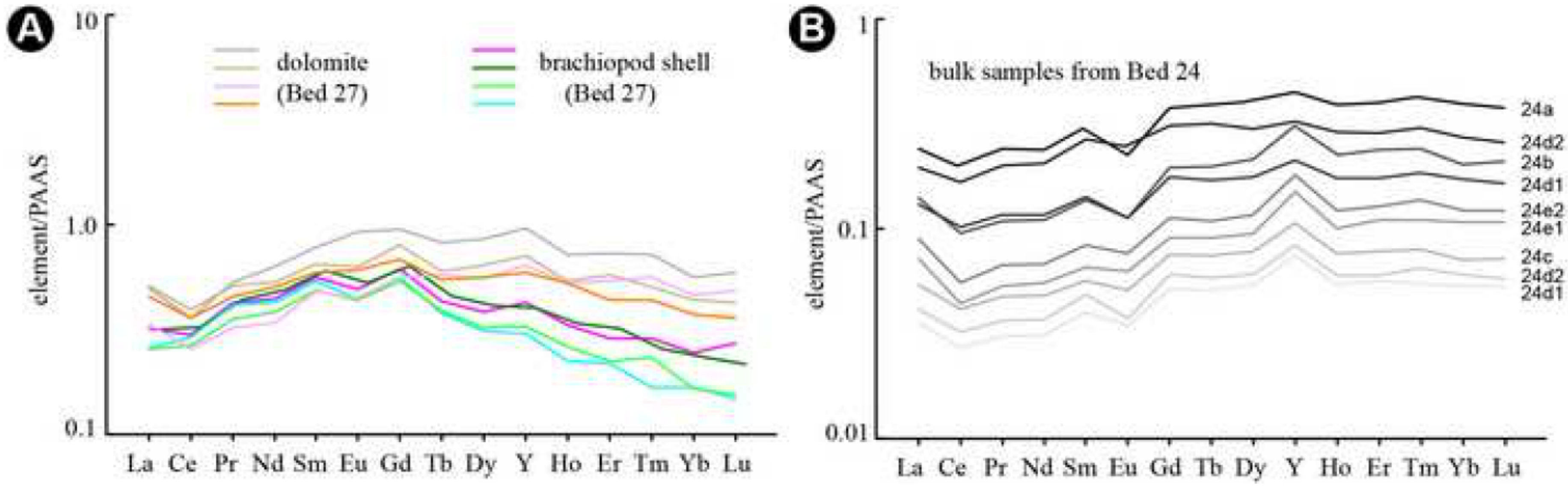

Figure
Click here to download high resolution image

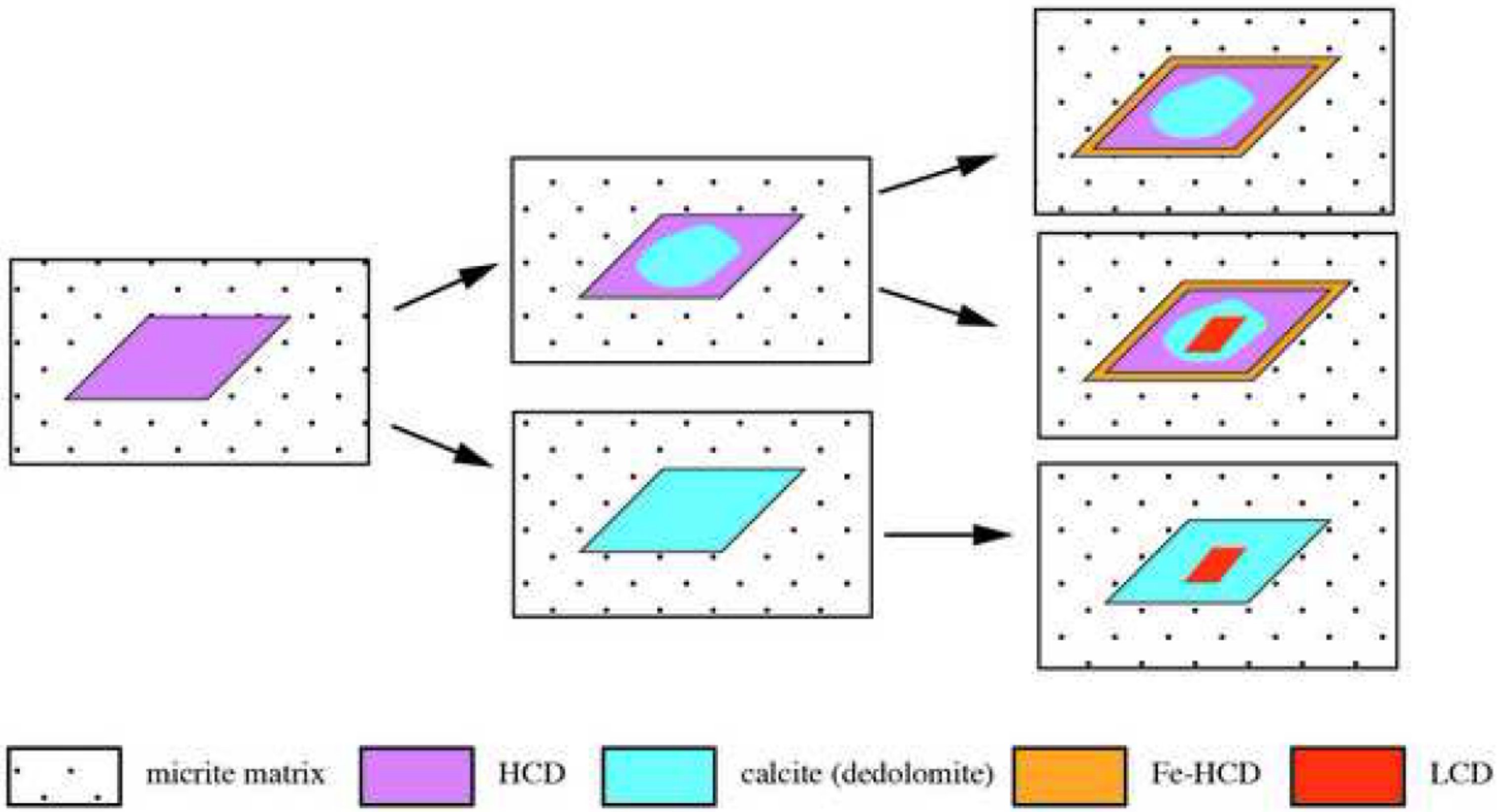

Figure

Click here to download high resolution image

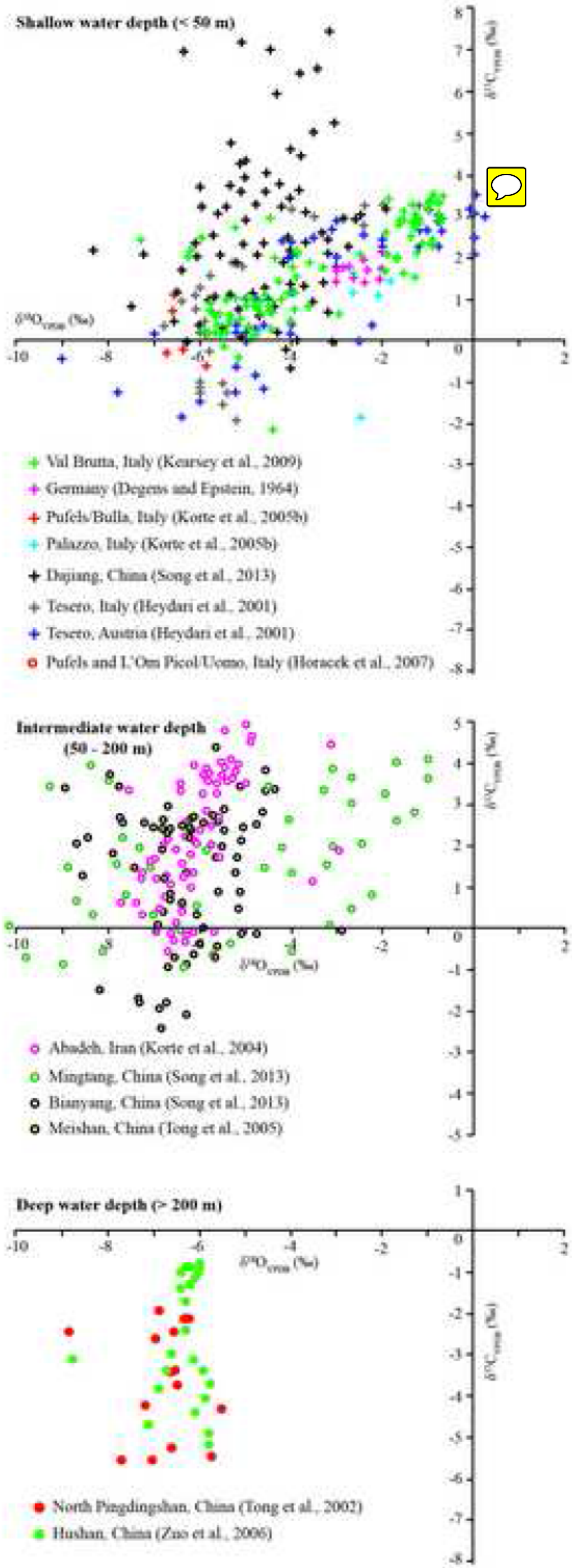

Table
Click here to download Table: Table 1.docx

Table 1. Summary of stable isotopic compositions and elemental data for carbonate rocks from Beds 24 to 62, Meishan section.

Bed	Sample	$\delta^{18}O_{cc}$ VPDB (‰)	$\delta^{13}C_{cc}$ VPDB (‰)	$\delta^{18}O_{dol}$ VPDB (‰)	$\delta^{13}C_{dol}$ VPDB (‰)	$\delta^{18}O_{bulk}$ VPDB (‰)	$\delta^{13}C_{bulk}$ VPDB (‰)	Sr (ppm)	Mn (ppm)	Mn/Sr
Bed 24	Bulk rock (24a)	-7.74	2.64	×	×	-7.74	2.64	429	254	0.6
	Bulk rock (24b)	-6.29	2.92	×	×	-6.29	2.92	404	245	0.6
	Bulk rock (24c)	-6.25	2.56	×	×	-6.25	2.56	689	118	0.2
	Bulk rock (24d1)	-7.19	2.44	×	×	-7.19	2.44	857	214	0.2
	Bulk rock (24d1)	-4.84	2.38	×	×	-4.84	2.38	746	169	0.2
	Bulk rock (24d2)	-5.50	2.36	×	×	-5.50	2.36	699	164	0.2
	Bulk rock (24d2)	-7.16	1.72	×	×	-7.16	1.72	424	475	1.1
	Bulk rock (24e1)	-5.05	2.25	×	×	-5.05	2.25	524	260	0.5
	Bulk rock (24e2)	-5.31	2.07	×	×	-5.31	2.07	563	260	0.5
Bed 26	Claystone	-7.82	-0.77	×	×	-7.82	-0.77	×	×	×
Bed 27	Bulk rock 27-I (1)	-7.31	0.13	×	×	-7.31	0.13	×	×	×
	Bulk rock 27-I (2)	-7.75	0.16	×	×	-7.75	0.16	×	×	×
	Bulk rock 27-I (3)	-8.09	0.18	×	×	-8.09	0.18	89	228	2.6
	27-II dark clast (1)	-5.58	1.33	×	×	-5.58	1.33	×	×	×

	27-II dark clast (2)	-6.20	0.94	×	×	-6.20	0.94	×	×	×
	27-II matrix	-7.12	-1.49	×	×	-7.12	-1.49	×	×	×
	Bulk rock 27-III (1)	-6.84	-0.37	-3.27	1.65	×	×	×	×	×
	Bulk rock 27-III (2)	-4.73	0.30	-2.12	1.88	×	×	×	×	×
	Bulk rock 27-III (3)	-4.99	0.60	-2.34	1.65	-4.99	0.89	231	592	2.6
	Bulk rock 27-IV (1)	-6.14	0.35	-2.64	2.03	×	×	×	×	×
	Bulk rock 27-IV (2)	-5.91	0.53	-2.12	1.95	×	×	×	×	×
	Bulk rock 27-V (1)	-5.95	0.19	-4.15	1.58	×	×	×	×	×
	Bulk rock 27-V (2)	-5.56	0.62	-2.35	1.79	×	×	×	×	×
	Bulk rock VI (1)	-7.26	-0.34	-4.23	3.52	×	×	×	×	×
	Bulk rock VI (2)	-6.56	-0.21	-5.35	1.43	×	×	×	×	×
	Bulk rock VI (3)	-5.95	0.19	-4.15	1.58	-6.07	0.50	186	606	3.3
Bed 28	Claystone	-7.78	-0.76	×	×	-7.78	-0.76	158	761	4.8
Bed 29	Bulk rock (29-1)	-6.60	-0.05	-3.82	1.57	-5.14	1.05	201	816	4.1
	Bulk rock (29-2)	-7.18	0.14	-2.61	1.95	-4.32	1.28	215	705	3.3
	Bulk rock (29-3)	-6.68	0.22	-3.29	1.46	-4.51	1.15	163	719	4.4
	Bulk rock (29-4a)	-6.05	0.52	-3.30	1.61	-4.83	1.17	189	749	4.0
	Bulk rock (29-4b)	-6.46	0.25	-3.38	1.43	-4.21	1.14	169	738	4.4
	Bulk rock (29-4c)	-7.66	-0.15	-3.36	1.27	-3.99	1.12	143	657	4.6

	Bulk rock (29-4d)	-7.00	0.11	-3.25	1.34	-4.20	1.08	126	536	4.3
Bed 30	Bulk rock	-6.88	-0.29	-6.61	-1.47	-5.89	-0.13	101	295	2.9
Bed 31	Bulk rock	-8.80	-0.59	-2.16	2.32	-6.46	0.17	98	367	3.7
Bed 33	Bulk rock (1)	-10.24	-0.47	-3.98	1.30	-7.83	0.36	294	367	1.3
	Bulk rock (2)	-8.98	-0.11	-4.06	1.30	-7.90	0.41	909	733	0.8
Bed 34	Bulk rock (1)	-9.07	-1.00	-1.79	1.86	-6.14	-0.20	108	932	8.7
	Bulk rock (2)	-7.06	0.05	-3.93	0.33	-5.71	0.07	234	571	2.4
Bed 35	Bulk rock	-4.69	-0.38	-2.27	1.50	-4.25	1.11	193	751	3.9
Bed 36	Bulk rock	-6.00	0.50	-2.57	1.39	-4.36	0.98	120	550	4.6
Bed 38	Bulk rock	-6.89	-0.13	-2.83	1.30	-4.57	0.93	114	502	4.4
Bed 39	Bulk rock	-5.70	0.76	-3.67	0.36	-8.58	0.20	75	413	5.5
Bed 42	Bulk rock	-7.56	-0.89	-3.30	-0.50	-6.36	-0.61	87	628	7.2
Bed 44	Bulk rock	-8.83	-0.27	-5.09	-0.65	-6.26	-0.71	73	451	6.2
Bed 45	Bulk rock	-7.58	0.40	-7.38	1.24	-6.72	-0.68	89	595	6.7
Bed 47	Bulk rock	-6.79	-0.80	-5.80	-0.17	-6.77	-0.57	81	516	6.4
Bed 52	Bulk rock	-8.78	0.09	-1.93	1.26	-6.77	-0.37	81	451	5.6
Bed 53	Bulk rock	-7.56	0.10	-6.23	4.11	-6.97	0.07	98	506	5.2
Bed 54	Bulk rock	-3.33	2.05	-3.93	0.38	-5.75	0.30	172	2180	12.7
Bed 56	Bulk rock	-6.25	0.85	-5.24	1.28	-6.83	0.98	194	885	4.6
Bed 57	Bulk rock	-7.09	1.73	-4.79	1.49	-6.60	1.10	121	439	3.6
Bed 58	Bulk rock	-6.29	1.07	-6.03	1.40	-6.91	1.09	262	1066	4.1
Bed 61	Bulk rock	-6.09	0.72	-5.51	1.10	-6.82	0.81	202	996	4.9
Bed 62	Bulk rock	-6.54	0.85	-5.52	1.53	-7.11	1.11	489	1064	2.2

Table
Click here to download Table: Table 2.docx

Table 2. The Sr, Mn, Fe, rare earth elements (REE) and Y concentrations of brachiopod shells, dolomite, and bulk limestones in Meishan section.

Bed	Sample	$CaCO_3$	$MgCO_3$	Sr	Mn	Fe	ΣREE	Y
		wt%	wt%	ppm	ppm	ppm	ppm	ppm
Bed 27	brachiopod shell	94	2	837	368	1016	65.5	11.5
	brachiopod shell	95	2	746	377	855	60.5	8.2
	brachiopod shell	94	2	782	462	1050	71.3	11.0
	brachiopod shell	95	2	755	369	947	56.2	8.9
	dolomite	28	15	174	465	8220	60.2	17.2
	dolomite	27	12	173	432	6241	80.7	16.0
	dolomite	42	23	267	704	14736	88.8	19.1
	dolomite	50	34	252	518	3321	93.1	25.9
Bed 24	Bulk rock (24a)	95	na	429	254	na	55.1	11.9
	Bulk rock (24b)	95	na	404	245	na	30.5	8.6
	Bulk rock (24c)	95	na	689	118	na	11.9	2.8
	Bulk rock (24d1)	98	na	857	214	na	27.4	5.6
	Bulk rock (24d1)	98	na	746	169	na	8.0	2.0
	Bulk rock (24d2)	97	na	699	164	na	9.3	2.2
	Bulk rock (24d2)	95	na	424	475	na	44.7	8.8
	Bulk rock (24e1)	97	na	524	263	na	18.1	4.8
	Bulk rock (24e2)	98	na	563	260	na	14.6	4.0